

THESIS FOR THE DEGREE OF DOCTOR OF TECHNOLOGY

Hydrodynamic flow for deterministic sorting of cell-membrane components

BJÖRN JOHANSSON FAST



CHALMERS

Department of Physics
CHALMERS UNIVERSITY OF TECHNOLOGY
Göteborg, Sweden 2016

Hydrodynamic flow for deterministic sorting of cell-membrane components

BJÖRN JOHANSSON FAST
ISBN 978-91-7597-355-5

©BJÖRN JOHANSSON FAST, 2016

Doktorsavhandlingar vid Chalmers tekniska högskola
Ny serie nr 4036
ISSN 0346-718X

Department of Physics
Chalmers University of Technology
SE-412 96 Göteborg
Sweden
Telephone + 46 (0) 31-772 10 00

Printed at Chalmers Reproservice
Göteborg, Sweden 2016

Hydrodynamic flow for deterministic sorting of cell-membrane components
BJÖRN JOHANSSON FAST
Department of Physics
CHALMERS UNIVERSITY OF TECHNOLOGY

Abstract

The biological membrane, an amphiphilic structure that is the barrier between the cell interior and exterior, is one of the vital building blocks of all cells. Not only does it define the outer boundaries of the cell, it also carries important biological function by virtue of the proteins and other molecules that constitute the membrane, the function of which is in turn intimately coupled to their association with the lipid-based membrane.

That the function of the protein is linked to its amphiphilicity necessitates preservation of the amphiphilic environment when probing the function of membrane associated proteins. The low expression levels of, even overexpressed, membrane proteins in a cell membrane crowded with many different types of proteins presents a barrier for direct studies of this class of proteins in their native membrane environment.

In the work leading up to this thesis, the aim has been to overcome some of these hurdles and enable membrane protein accumulation and purification in a near native cell membrane. In the articles appended to the thesis, steps have been taken towards being able to move, concentrate, purify and in the end visualize single membrane proteins, using a combination of surface-sensitive imaging, microfluidics and hydrodynamic flow. The last development led to the insight that using this approach we were able to determine the exact size of nanometer-sized objects bound to the two-dimensional interface that is the supported membrane by measuring both the nanoparticles' deterministic and stochastic movement.

Looking forward, this thesis work has provided a solid foundation for deterministic sorting of membrane proteins, without the need for detergent solubilization. While this in itself is rather enticing, the possibility to simultaneously determine both the size and the biomolecular content of biological nanoparticles, as demonstrated in the final paper, might help telling whether it is the size, the amount of a specific molecule, or a precise combination of the two, that is decisive for their biological function, such as; infectivity, gene transfer or drug delivery in the context of virions, exosomes and nanoscale drug carriers, respectively.

Keywords: Supported lipid bilayer · Hydrodynamic forces · Microfluidics · Protein enrichment · Diffusion · Single particle tracking · Gold nanoparticles · Size determination · Native membrane vesicles

Appended papers

Paper I:

Hydrodynamic separation of proteins in supported lipid bilayers confined by gold barriers

Björn Johansson, Thomas Olsson, Peter Jönsson and Fredrik Höök
Soft Matter **9**, 9414–9419 (2013).

Paper II:

Label-free measurements of the diffusivity of molecules in lipid membranes

Björn Johansson, Fredrik Höök, David Klenerman and Peter Jönsson
ChemPhysChem **15**, 486–491 (2014).

Paper III:

Detergent free affinity purification of membrane proteins in supported native membranes

Björn Johansson Fast, Anders Lundgren, Stephan Block, Anders Gunnarsson, Stefan Geschwindner and Fredrik Höök
In manuscript

Paper IV:

Two-dimensional flow nanometry of biological nanoparticles for accurate determination of size and emission intensity

Stephan Block, Björn Johansson Fast, Anders Lundgren, Vladimir P. Zhdanov and Fredrik Höök
In manuscript

Contributions to appended papers

Paper I:

The concept was an idea of PJ and FH. This was further developed by BJ, who decided to use gold as the barrier material. The surface preparation was mainly done by BJ and the experiments were planned and executed by BJ and TO. The data analysis was done by BJ with help from PJ. BJ wrote the majority of the manuscript, with help from TO. PJ and FH provided feedback during the writing process and wrote parts of the manuscript.

Paper II:

The experiments were based on previous work done PJ, using a micro-pipette to accumulate membrane-associated proteins. BJ and PJ planned the execution of the experiments, after which BJ applied for funding to visit PJ in Cambridge, UK, where the experiments were carried out together with PJ. PJ did most of the data analysis, with BJ helping where suitable. BJ and PJ wrote the manuscript with feedback from FH and DK.

Paper III:

The idea emerged from discussions between BJF and AL, after failed attempts at performing experiments where the wanted outcome was similar. AL was responsible for designing the gold nanoparticles and biotinylation of anti-bodies and proteins. BJF was responsible for the microfluidic device, and running the experiments. AG provided the biological material and did the SDS-PAGE and Western blotting. SB did the theoretical work and wrote the scripts used for analysis. The majority of the manuscript was written by BJF, with help from all other coauthors, but primarily from AL.

Paper IV:

As a continuation of Paper III and work done by SB, the idea behind the method presented in paper IV is a collective effort between all authors. Samples used for size determination were prepared by AL (vesicles and gold nanoparticles), SB (vesicles) and BJF (gold nanoparticles). BJF was responsible for the microfluidic device and for running the experiments and collecting the data. SB did the theoretical work with input from VZ and wrote the scripts used for analysis. The manuscript was mainly written by SB with BJF, AL, VZ and FH contributing where suitable.

Contents

1	Introduction	1
2	Background	5
2.1	Lipids and lipid membranes	5
2.1.1	The lipid molecule and self-assembly	5
2.1.2	Vesicles and supported membranes	6
2.1.3	Native-derived supported membranes	9
2.2	Diffusivity and single particle tracking	10
3	Methods	13
3.1	Optical microscopy	13
3.1.1	Fluorescence microscopy	13
3.1.2	Label-free microscopy techniques	17
3.1.3	Acquisition and resolution	20
3.2	Microfluidics and hydrodynamic forces	22
3.2.1	Shear-driven lipid bilayers	22
3.2.2	Hydrodynamic kiting	24
3.2.3	Hydrodynamic trapping	28
3.3	Synthesis and functionalization of gold nanoparticles	30
3.4	Size determination of nanometer sized objects	33
3.4.1	Nanoparticle tracking and analysis	33
3.4.2	Scanning electron microscopy	34
3.4.3	Two-dimensional flow nanometry	35
4	Summary of results and reflections	39
4.1	Paper I	39
4.2	Paper II	42
4.3	Paper III	44
4.4	Paper IV	48
5	Outlook - deterministic sorting	53
	Acknowledgements	55
	Bibliography	57

List of abbreviations

BACE1	β -secretase 1
Biotin-PE	1,2-dipalmitoyl-sn-glycero-3-phosphoethanolamine-N-(cap biotiny)
CD2	Polyhistidine tagged extracellular rat CD2
CD2-488	CD2, Alexa Fluor® 488 Conjugate
CTB	Cholera toxin B subunit
DGS-NTA	1,2-dioleoyl-sn-glycero-3-[(N-(5-amino-1-carboxypentyl)iminodiacetic acid)succinyl] (nickel salt)
FRAP	Fluorescence recovery after photobleaching
G_{M1}	Monosialotetrahexosylganglioside
His-tag	Hexa histidine-tag
LSPR	Localized surface plasmon resonance
NA	Numerical aperture
Ni-NTA	Nickel-nitrilotriacetic acid
NMV	Native membrane vesicle
PDMS	Polydimethylsiloxane
PEG	Poly(ethylene)glycol
PLL	Poly-l-lysine
POPC	1-palmitoyl-2-oleoyl-sn-glycero-3-phosphocholine
R-DHPE	Lissamine rhodamine B 1,2-dihexadecanoyl-sn-glycero-3-phosphoethanolamine
SA	Streptavidin
SA-488	Streptavidin, Oregon Green® 488 Conjugate
SEEC	Surface enhanced ellipsometric contrast
SEM	Scanning electron microscope
SLB	Supported lipid bilayer
SNR	Signal to noise ratio
SPT	Single particle tracking
SUV	Small unilamellar vesicle
TIRF	Total internal reflection fluorescence microscopy

Chapter 1:

Introduction

An approximately 5 nm thick amphiphilic fluid mainly consisting of lipids is the barrier between the cell interior and exterior.^[1] Both the cell interior and exterior is an aqueous environment, but the cell-membrane interior is hydrophobic, and this hydrophobicity is an efficient barrier hindering passage of water soluble molecules into and out of the cell. However, the cell-membrane is not only a membrane; while lipids constitutes the largest number of molecules in the membrane, many molecules that reside in the membrane are involved in cell signaling and in transport of molecules across the membrane.

These molecules of the cell-membrane belong to a wide variety of classes, ranging from lipids via carbohydrates to proteins. Their location on the cell periphery, where they are easily accessible for the outside world, is not only vital for the cell, but viruses and toxins have through evolution developed to take advantage of them to allow entrance to the interior of the cell. That many membrane proteins are involved, primarily as receivers, in cell-signaling makes them very interesting from a pharmaceutical point of view, since by learning to manipulate the membrane proteins, many of the processes in the cell can be controlled. In fact, more than 50 % of all pharmaceuticals on the market today target a membrane protein.^[2] Despite this obvious significance, the inherent difficulty associated with studying the function of membrane proteins limits our knowledge about them.

These challenges mainly revolve around the amphiphilicity inherited from the cell-membrane in which they reside, making them insoluble in water. In contrast to lipids, proteins are chains of amino acids that fold into a three-dimensional structure by primarily hydrophobic interactions. The function of a protein is mainly dependent on two things, the amino acid sequence and the structure into which it has folded. Hence, the structure of a protein is important to study, but in the case of a membrane protein this is very difficult. Since the protein structure is the result of energy minimization in the presence of a cell-membrane, and since pulling the protein out of the membrane changes the energy landscape that the protein experiences, the amino acid chain will refold into a structure that is more energetically favorable given the new environment premisses. In doing so, the protein will almost inevitably lose its function. Additionally, this process is often irreversible.^[3] This process is called denaturation, and while it was the result of placing a membrane protein in an aqueous solution in the example above, it can also be the result of a temperature increase, a change in the ionic strength, pH or polarity. For example, increasing the temperature increases the energy of the atoms in the protein and they thus become less likely to stay in their designated place. At high enough temperature, the result is denaturation and

is something most people have experienced first hand, frying an egg.

Moreover, in studying proteins it is often beneficial if they exist in large quantities and concentrations far higher than what is common in nature. Such an abundance is difficult to acquire in a natural system, since the cell and the cell membrane constitutes complex mixtures of molecules and are very crowded. For water soluble proteins, this challenge has been mastered, they can be purified using *e.g.* gel filtration. The techniques developed for purification of water-soluble proteins have proven so effective that most of the available protocols for purification of membrane proteins rely on making the amphiphilic proteins water soluble, often accomplished by detergent solubilization. While this often works in the solubilizing step, the membrane proteins must be reconstituted into a new membrane environment post purification for many types of measurements of *e.g.* to study their activity. One of the aims of this thesis work has been to eliminate the need for detergent solubilization by development of means to isolate and handle membrane proteins without removing them from their natural environment.

While this accepted challenge is a difficult one, it has been explored with partial success. One of the first successful in-membrane protein separation experiments was performed by Poo and Robinson, whom in 1977 managed to locally accumulate membrane molecules on the surface of a single cell using electrophoresis.^[4] Performing membrane protein separation on a single cell, however, limits the achievable separation to the dimension of the cell (*i.e.* a couple of μm), and this is part of the reason why continuous macroscopic planar membranes, such as the supported lipid bilayer (SLB) have gained traction in this field.

Both labeled and label-free detection systems have been used in this thesis work, with an explicit comparison between the two provided in paper II. Both approaches have their set of advantages and disadvantages. The use of fluorescent labels generally renders increased sensitivity and simplify readout tremendously in for example biological imaging^[5] as well as diagnostics (*e.g.* ELISA).^[6] The use of fluorescent labels, however, does inevitably mean that an unnatural modification must be incorporated in the system; after all, the number of natural fluorophores is low (the green fluorescent protein found in the jellyfish *Aequorea victoria*, and derivatives thereof, deserves to be mentioned due to the strength of their fluorescence). In particular, the coupling of a fluorophore to a system means incorporation of a potential risk to induce unspecific interactions and altered function of the modified system, not least due to hydrophobic interactions between fluorophores. So while fluorophores paves the way for easy analysis in some systems, the fluorophore itself can yield false positives. The use of a label-free measurement technique would be advantageous in those cases. However, many of the available label-free measurement techniques that exist (such as *e.g.* surface plasmon resonance) have disadvantages, such as a lack of single molecule resolution, that make them difficult to use or even unsuitable to study, in particular, cells or cell membranes. Moreover, not all molecules are easy, or even possible, to label. This may be due to that the only place to put the label happens to coincide with the active site of the molecule, and thus labeling the molecule renders it inactive. For systems where the molecules are such, label-free methods, regardless of their sensitivity, is the only option.

In this thesis work a further extreme of labeling has also been investigated; conjugation of gold nanoparticles to preselected molecules of interest in the membrane. These gold nanoparticles, while small, are huge in comparison to the proteins to which they are bound. The choice might seem odd, but is an effect of the hydrodynamic force acting on the nanoparticle when subject to a bulk flow in a microfluidic device, which is orders of magnitude larger than the force acting on molecules in the membrane, allowing for induction of directed movement of the pre-selected molecule of interest which can be utilized to enrich the molecule of interest, as seen in paper III.

Continuing on the subject of nanoparticles tethered to a supported membrane; rounding up the thesis in paper IV is a size determination method for nanoparticles tethered to a fluid support; two-dimensional flow nanometry, which utilizes most of the techniques and methods developed during this thesis work. The size of an object is often such a blatantly obvious characteristic of the object that it runs the risk of neglect when the object is characterized. However, with the recent increased interest in a category of biological nanoparticles known as exosomes, size has become a defining parameter, with nanoparticles qualifying as exosomes only if they are within a, heavily debated, size range.^[7] The two-dimensional flow nanometry method that is introduced in chapter 3 and paper IV, could help determining whether it is the size or the amount of a specific molecule, or, indeed, a specific combination of both, that is the decisive factor determining the function of biological nanoparticles.

The aim of this thesis is to provide a summary of the experimental work that has been performed leading up to this thesis and to provide an introduction to the papers appended to this thesis. The thesis consists of five chapters, this introduction being the first. After the introduction follows the background, where the lipids, lipid vesicles, supported membranes and single particle tracking is discussed. These are the fundamentals on which this thesis is built. After the background follows the methods, presenting the microscopy techniques that have been used to visualize vesicles, bilayers, proteins and gold nanoparticles. After that follows a discussion on microfluidics, by which hydrodynamic forces have been applied to both supported membranes and objects attached to supported membranes. The synthesis of gold nanoparticles is also included in this chapter together with a discussion on three different size determination techniques; nanoparticle tracking and analysis, scanning electron microscopy and two-dimensional flow nanometry. After the background and methods chapters, the results from the appended papers where these methods have come to use are briefly discussed in chapter 4, before I try my hand at fortune-telling, introducing the concept of deterministic sorting as the future outlook of this thesis work.

Chapter 2:

Background

2.1 Lipids and lipid membranes

Lipids, a group of amphiphilic – part hydrophilic, part hydrophobic – molecules that include phospholipids, glycolipids, cholesterol and fatty acids, are the main constituents of biological membranes and many of the properties of the cell membrane are inherited from the properties of the lipids it constitutes. In fact, the hydrophobic interaction between the hydrophobic tails of lipids is one of the major driving forces in membrane formation.^[8]

2.1.1 The lipid molecule and self-assembly

To understand why lipids self-assemble in an aqueous solution, we need to look at the structure of a lipid molecule, in this case, we will look at a phospholipid. These lipids have a hydrophilic head-group and a hydrophobic hydrocarbon tail, schematically shown in Fig. 2.1. In the presence of an aqueous solution, the hydrophobic hydrocarbon chains give rise to self-assembly by hydrophobic interaction. The nature of the self assembly process depends on the structure of the lipid, which is described by three parameters: the optimum head-group area, a_0 , the critical chain length, l_c , and the hydrocarbon volume, v .^[9] The optimum head-group area corresponds to the distance between amphiphilic molecules that minimizes the free energy. A too large distance means that the hydrophobic hydrocarbon chains are forced into contact with the surrounding water molecules, while a too small distance means that the head-groups repel each other due to for instance electrostatic forces. The critical chain length is the length of the hydrocarbon chain, in a fully extended configuration, while the hydrocarbon volume simply is the volume of the hydrocarbon chains.^[8;9] These three parameters can be combined into a dimension-less quantity known as the critical packing parameter (CPP);

$$\text{CPP} = \frac{v}{a_0 l_c}, \quad (2.1)$$

a geometric characterization of the lipid molecule, in turn yielding the lipids preferred self-assembled structure, see Fig. 2.2. A CPP below 1/3 corresponds to a cone-shaped lipid with a large head group and a short hydrocarbon tail. One example of such a lipid is the commonly used detergent sodium dodecyl sulfate (SDS). These low CPP-lipids tend to form spherical micelles. A slightly higher CPP, between 1/3 and 1/2 corresponds to a truncated cone and such lipids will primarily form cylindrical micelles. As the CPP approaches 1 (these are often lipids with dual hydrocarbon chains as illustrated in Fig. 2.2) lipids will tend more towards formation of lipid

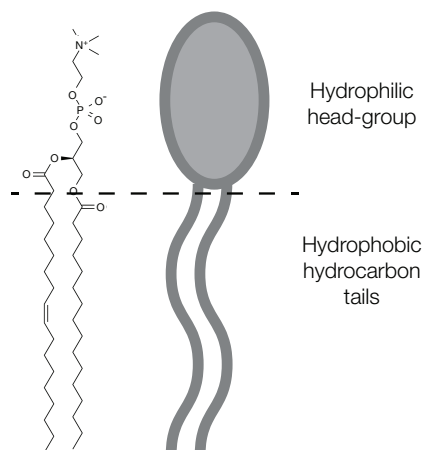


Fig. 2.1: The POPC molecule and a schematic interpretation. The hydrophilic and hydrophobic parts have been indicated.

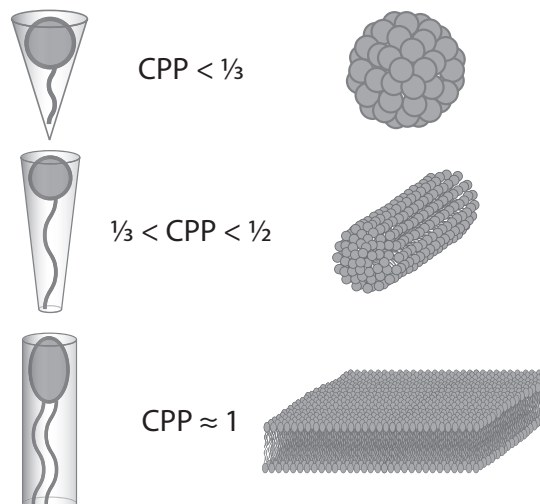


Fig. 2.2: A schematic illustration of the critical packing parameter, CPP, a geometrical characterization of lipids. A small CPP corresponds to the lipids being cone-shaped and such lipids tend to aggregate into spherical micelles. As the CPP increases, the lipid geometry changes to first a truncated cone and then a cylinder and the corresponding lipid self-assembly structures changes from cylindrical micelles to lipid bilayers.

bilayers, two large sheets of lipids with the hydrophobic hydrocarbon chains facing each other, and the hydrophilic head-groups exposed to the aqueous environment. The lipid bilayer can not only have the shape of a planar membrane, but for instance also form a spherical shell, called a lipid vesicle or liposome. These vesicles exist both as unilamellar, a single spherical shell, and multilamellar, multiple concentric shells with different radii in a layered structure.^[9]

2.1.2 Vesicles and supported membranes

The lipid vesicle, or liposome, has been fundamental for the work performed in this thesis, mainly due to certain properties of small unilamellar vesicles (SUV). For example, upon reaching a critical surface coverage when adsorbing to a glass surface, these vesicles will start to rupture and form a continuous supported lipid bilayer (SLB). In essence, the SLB is a two-dimensional fluid that maintains its continuity over large areas. While artificially created membranes come in different shapes, for instance painted or black lipid membranes^[10;11] and droplet-on-hydrated-support bilayers.^[12], the conveniency with which SLBs can be formed has made them the platform of choice for the separation applications explored in this work.

When working with SLBs, the choice of support is critical since an SLB only can be formed on a limited number of surfaces, most notably glass coverslips and

other silica surfaces.^[13-16] One way to form an SLB is to first prepare a suspension of lipid vesicles. The vesicles can be formed by extrusion of a lipid containing aqueous suspension through a porous membrane^[17;18] or by ultrasonication of the suspension using *i.e.* a sonication probe^[19] or sonication bath.^[20] The lipid vesicle suspension is subsequently placed in contact with the surface, whereupon the lipid vesicles reach the surface through diffusion. When reaching the surface the lipids adsorb if the attraction is sufficiently large and when a sufficiently high surface coverage is reached, they start to rupture and spread onto the support, if certain conditions are fulfilled. These conditions include the material and the cleanliness of the surface.^[21-25] It has been proposed that the point of rupture on the vesicle is where the radius of curvature is smallest.^[26] This rupturing process continues, and is accelerated in an autocatalytic manner,^[23] until the entire surface is covered with an SLB. The formation of an SLB is shown schematically in Fig. 2.3. In Fig. 2.3(b), the rupturing vesicle is shown to rupture at the point where the curvature is highest.^[27] However, the way a vesicle ruptures is a debated subject, with evidence of both the method shown in Fig. 2.3(b) as well as the so called parachute model,^[28;29] where the vesicle rupture happens at the vesicle-vesicle contact points.^[27] The large difference between these two methods for vesicle rupture is the orientation of the supported membrane after the rupture where the first procedure yields a supported membrane where the upper leaflet primarily originating on the inside of the vesicles whereas it is primarily the outside of the vesicles that becomes the upper leaflet in the second procedure. While not the prime aim of either of the studies presented in this thesis, the indirect results presented in paper III, where a supported membrane is formed from a gold nanoparticle-vesicle construct where the gold nanoparticle is attached to the outside of the vesicle. Thus, if lipid vesicles form an SLB via rupturing at the point of highest curvature, a low number of mobile gold nanoparticles is to be expected since the gold nanoparticles would end up on the lower leaflet – below the SLB. If, on the other hand, vesicles rupture at vesicle-vesicle contact points, a larger number of mobile gold nanoparticles is expected, since the gold nanoparticles would preferentially be on the upper leaflet. In the discussed experiment $\sim 40\%$ of the observed gold nanoparticles were mobile after rupture and hence, these results do not prove any of the explanation models. Perhaps the best explanation is that there is some credibility to both.

The SLB, formed according to the process described above, is built up by two sheets of lipids on a solid support. Between the lower leaflet and the support is a hydrating film of on the order of 1 nm.^[30-34] The close proximity of the support, less than half the length of a lipid, influences the SLB and molecules bound to the bilayer, *e.g.* molecules that protrude from the bilayer may not fit in the small space between the support and the bilayer or their diffusivity may be considerably lower than would otherwise be the case.^[25;35] Polymer cushions of different types have been used to mitigate this limitation, either creating a softer gel-like surface or increasing the distance between the SLB and the surface.^[36;37]

Each of the two sheets of the lipid bilayer can be described as a two dimensional liquid with a diffusibility.^[38] It has been shown that the diffusivity of the SLB is comparable to that of a free membrane, but on the order of a factor two lower.^[39;40] The diffusivity in the membrane is also related to the cleaning protocol for the sur-

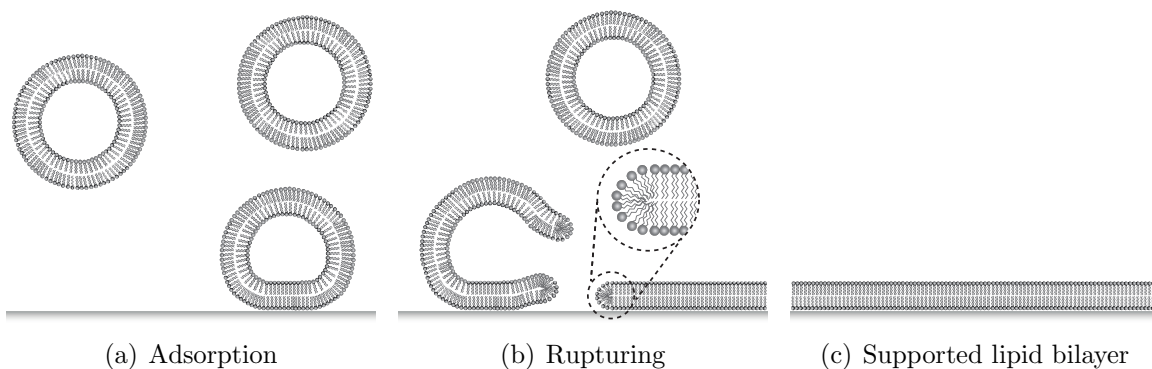


Fig. 2.3: A schematic illustration showing the formation of an SLB. (a) Lipid vesicles adsorb on the surface. (b) When a certain area fraction is covered with lipid vesicles, the vesicles start to rupture into a more energetically favourable planar bilayer structure. The magnified view shows the situation on the membrane edge. (c) The rupturing process will continue until the entire surface is covered with an SLB.

face,^[41] the temperature,^[42;43] and the concentration of ions in the solution.^[44;45] The sheets are connected at the edges of the SLB (or smaller SLB sheets) where the upper and lower leaflet wrap, keeping water out of the hydrophobic bilayer interior, shown schematically in the magnified view in Fig. 2.3(b). However, for the cylindrical shaped, bilayer forming, lipid discussed in this thesis, the energy associated with an edge is larger than the energy of the flat regime, in particular due to two effects. First, the large curvature at the edge tends to push the hydrophilic head-groups apart, forcing the hydrophobic hydrocarbon chains into contact with the surrounding water. Second, the curvature forces the hydrocarbon chains closer together, causing steric hindrance, further increasing the energy associated with the edge.^[9;23] It is thus not very pleasant for a lipid to sit at the membrane edge, and the energy increase associated with the membrane edge as compared to a flat region is the reason lipid vesicles form. A vesicle, being a spherical shell has no edge, but there is an energetic penalty associated with the vesicle's curvature. In a homogenous lipid mixture, the penalties associated with the membrane edge and the vesicle curvature, together with surface implications, govern SLB formation. By using non-homogenous lipid mixtures or membrane protein scaffolds however, these apparent rules may be circumvented, as proven for instance by lipid nanodiscs.^[46]

While created in different manners, all of the mentioned artificially created lipid membranes, as the name states, share the lipid element. The lipids that constitute the membrane can differ, but the lipid composition is generally, with few exceptions,^[47] simpler than that of a biological membrane. The advantage of an artificially created membrane is twofold. Firstly, specific functionality can be added to the membrane, by lipids, cholesterol and reconstituted proteins, such that only one or a selected number of specific aspects of the membrane can be studied. Secondly, in contrast to the cell, there is nothing apart from the size of the measurement device that limits the size of the lipid membrane, which gives larger opportunities for *e.g.* separation of membrane-bound species, as discussed in the next chapter.

Structurally, although not necessarily functionally, a lipid bilayer resembles one of the most important building blocks of all things living; the biological cell membrane. The cell membrane is the barrier between the cell and the surroundings but also acts as a boundary of the internal organelles of cells and is a very complex structure involving thousands of different types of lipids, proteins, carbohydrates and other molecules.^[1] Those molecules regulate many of the processes that takes place within the cell and are therefore a necessary ingredient for life. However, while required in a living system, the complexity of the real biological membrane, with lipids, proteins and carbohydrates, and the membrane interaction with the cellular skeleton and extracellular matrix as well as the curvature of the cell, make direct investigations of specific aspects of biological membranes, such as properties of a single protein or the membrane itself, very difficult.^[38] Significant fundamental knowledge about biological membranes can however be gained from the study of a suitable model system in lieu of the famous Einstein quotation “Make everything as simple as possible, but not simpler”. One such simplistic model system is the artificially created lipid bilayer made up from primarily synthetically fabricated lipids or purified biologically produced lipids.^[22;25;38;48;49]

2.1.3 *Native-derived supported membranes*

Artificially created lipid bilayers can go a long way towards understanding the cell membrane, from a bottom up perspective. However, if the study of more complex systems are of interest, using artificially created systems are a lot of bother. In the bottom-up approach discussed in the previous section, components are added one after the other meaning that in order to have something that resembles a natural system, a large number of components must be added.

If a more complex system is of interest, a top-down, rather than bottom-up, approach is advised. Instead of adding components to make the system more complex, as is the case in the bottom-up approach, the top-down approach is the opposite; start with something as close to a native cell-membrane as possible. While this sounds relatively straight forward in theory, creation of a top-down supported membrane has been a challenge. The issue lies in the lipid diversity, cholesterol content and high protein content of a native cell-membrane, all of which impair membrane formability by vesicle rupture on a substrate.^[47;50–54] Several methods have been suggested to overcome this challenge, among them are co-adsorption of synthetic vesicles and NMVs,^[55;56] using the catalytic rupture induction of a rolling membrane edge,^[47;52] and single α -helical peptides.^[53]

Further, even if formation of a supported membrane from NMVs was successful, the mobility of both lipids and proteins in the supported membrane has proven impaired, in the extent of proteins with protruding domains to the extent of insignificant mobility.^[57] A recent development of the co-adsorption method, where NMVs are mixed with synthetic vesicles and sonicated before formation of the supported membrane has proven promising, especially when the synthetic vesicles contain a small fraction of PEG-modified lipids.^[57] The presence of PEG has dual purposes. First, it facilitates fusion of coalesced vesicles during the ultra-sonication.^[58] Further, when the supported membrane has formed, the PEG forms a cushion, lifting the supported

membrane off of the substrate, enabling mobility of membrane proteins and other membrane material extending beyond the lipid base.^[37]

2.2 Diffusivity and single particle tracking

The concept single particle tracking (SPT) has been crucial to papers III and IV, where it was used to extract the diffusivity of single membrane proteins and the size of nanoparticles respectively. While the name gives part of the concept away, it is perhaps less obvious that the diffusivity, and in the extension the size of a particle, can be determined by tracking it.

To understand how this can be done, let's first discuss what diffusion is and why objects diffuse. Consider a particle in an aqueous solution, but before looking at the particle, let's have a look at the aqueous solution. The aqueous solution consist of molecules, for simplicity, assume that all these are water molecules. All the water molecules of the solution are in constant movement, a movement characterized by rapidly changing velocities due to collisions between molecules. The movement stems from the equipartition theorem, according to which there is a thermal energy of $\frac{1}{2}k_B T$ per degree of freedom.* The thermal energy is thus on the order of $k_B T$, which at room temperature is approximately 25 meV – not insignificant for something as small as a water molecule.

Going back to the particle in the aqueous solution, the rapidly moving water molecules will collide with the particle, hitting it from all sides and these collisions will cause the particle to move randomly, performing a so called random walk, see Fig. 2.4(a). The random movement of a particle in an aqueous solution was first observed by Robert Brown in 1827, when he put an aqueous solution containing pollen grains under the microscope and could see the random movement of particles trapped in cavities in the pollen grains. While Brown could observe the movement, he did not have an explanation of the underlying mechanism. 78 years after the first documented observation of Brownian motion, Albert Einstein published a paper in 1905, in which he explained that the motion of a particle in an aqueous solution was, in fact, due to collisions with the water molecules in the fluid.

What Einstein[†] presented was that the diffusion coefficient of a particle undergoing Brownian motion is related to the mean squared displacement of the particle. The mean squared displacement of a particle is defined as the deviation of the particles

*There are generally three types of degrees of freedom; translational, rotational and vibrational. For the water molecule this yields a maximum of 9 degrees of freedom. However, two of the three vibrational degrees of freedom require too high energy to be excited at room temperature and likewise does one of the rotational. The water molecule at room temperature thus has 6 degrees of freedom and a thermal energy of $E = 3k_B T$.

[†]Brownian motion was independently characterized by Albert Einstein^[59] and William Sutherland^[60] in 1905 and Marian Smoluchowski^[61] in 1906, but Einstein is usually the one credited as the more detailed explanation of the mechanism, despite Sutherland's work being published ahead of Einstein's.

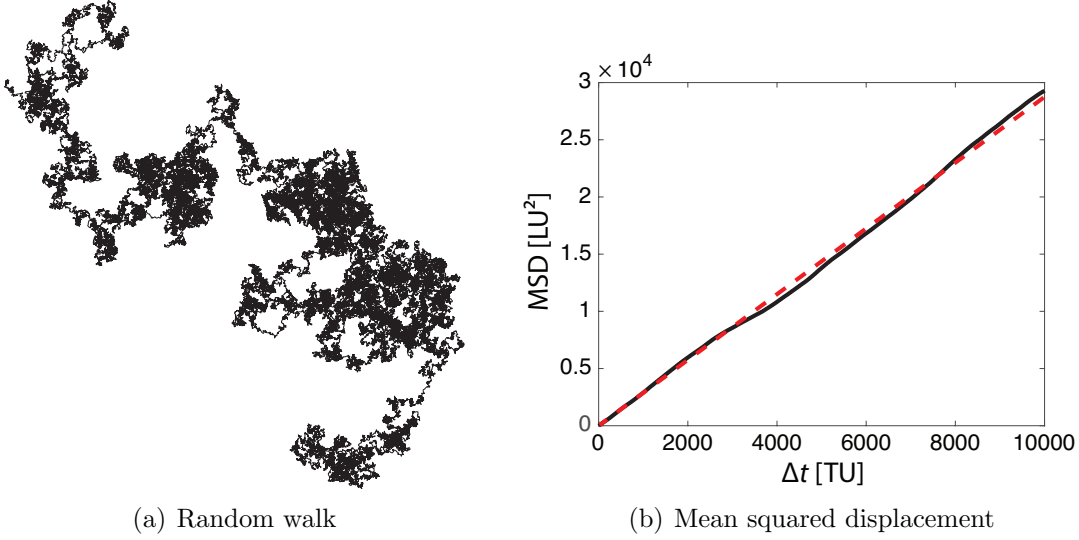


Fig. 2.4: (a) An illustrative random walk as performed by one random walker and in (b) the resulting mean squared displacement as calculated with internal averaging using a rolling time window of Δt ranging from 1 to $\tau_{\max}/10$. Dashed in red is shown a linear fit, from which the diffusivity can be calculated.

position from a reference position,

$$MSD = \langle (x - x_0)^2 \rangle = \frac{1}{\tau} \sum_{t=1}^{\tau} (x(t) - x_0)^2, \quad (2.2)$$

where x_0 is the reference position, $x(t)$ is the particles position at time t and τ is the time the average is taken over. What Einstein found was that the diffusivity scales linearly with the mean squared displacement at time t according to:

$$\langle (x(t) - x_0)^2 \rangle = q_d D t, \quad (2.3)$$

where $q_d = 2 \cdot dim$, is a dimension-dependent proportionality constant. Taking the random walk in Fig. 2.4(a) as an example, calculating the mean squared displacement using internal averaging with a rolling window of $\Delta t \in (1, \tau_{\max}/10)$ yields the mean squared distance as a function of Δt as presented in Fig. 2.4(b). Fitting the mean squared displacement with a linear function yields the red curve in Fig. 2.4(b) with a proportionality factor of 2.87. Since the particle performed a two-dimensional random walk, $q_d = 4$, and the diffusivity of the random walker in Fig. 2.4(a) is thus $D = 0.72 \text{ LU}^2/\text{TU}$.

In addition to this, Einstein also proved that the stochastic force that is the sum of the force from all water molecules colliding with the particle, cause drag if the particle is pulled through the fluid, explained by the fluctuation-dissipation theorem[‡]

[‡]The fluctuation-dissipation theorem was not yet stated when Einstein presented his work, but was originally formulated for electrons by Harry Nyquist in 1928. Briefly, it states that the an object in equilibrium with its environment will receive as much energy from the environment as it dissipates to it.

for Brownian motion:

$$D = \mu k_{\text{B}}T, \quad (2.4)$$

where μ is the particle's mobility, defined as $v = \mu F$ with v being the velocity resulting from application of the force F . At low Reynolds numbers the particle mobility is the inverse of the drag coefficient $\zeta = 6\pi\eta r$, where η is the dynamic viscosity of the medium and r is the hydrodynamic radius of the particle. Inserting $\mu = 1/\zeta$ in eq. 2.4 yields

$$D = \frac{k_{\text{B}}T}{6\pi\eta r}, \quad (2.5)$$

known as the Stokes-Einstein relation.

Combining determination of the diffusivity by measuring the mean squared displacement of a particle with the Stokes-Einstein relation, it is thus possible to extract the hydrodynamic size of a particle in solution by single particle tracking. As described in chapter 3 and paper IV, this thesis work culminated in a new method to determine the size of nanoparticles tethered to a mobile lipid bilayer, despite the fact that their diffusivity when tethered to an SLB is determined by the diffusivity of the linker in the SLB rather than by collisions with the surrounding water molecules.

Chapter 3:

Methods

3.1 Optical microscopy

Optical microscopy has been central to the work presented in this thesis, being the primary data acquisition tool. Optical microscopes come in many different variants, the most important ones for this work are of the inverted type where the sample is imaged from below, through a transparent substrate. Originally invented by J. Lawrence Smith in 1852,^[62] an inverted microscope is particularly useful when imaging things present on the bottom of a container,^[5] thus imaging of supported biological membranes is very suitable to the inverted microscope.

3.1.1 Fluorescence microscopy

The subjects of study in this thesis, lipids, proteins and nanoparticles, are too small to visualize directly using conventional optical microscopy *per se*. In microscopy in general, an image of a subject is the result of interaction (by means of *e.g.* refraction, reflection, absorption and scattering) between the subject and some illumination source. In optical microscopy the illumination source is photons. In electron microscopy it is electrons. Objects that are very small in comparison to the wavelength of the illumination source, such as those studied in this thesis work, do not interact sufficiently with the irradiating photons for the captured image to contain visible information of the interaction. They are invisible using optical microscopy, unless means are taken to eliminate background information.

One way to visualize the small entities is by using fluorescent labels. A fluorescent label is a molecule with an energy gap between the ground state, S_0 , and the first excited state, S_1 , that corresponds to the energy of a visible light photon. This means that the fluorophore can absorb an incoming photon with approximately the energy of the energy gap, see Fig. 3.1. This process leaves the fluorophore in an excited state,



The excited state, however, is not a stable state and to lower its energy, the electron will strive towards the ground state. The different relaxation processes by which the electron can approach the ground state have different transition rates. For instance, the low energy vibrational relaxation (heat) to the bottom of S_1 occurs more frequently than the larger energy photon emission relaxation between states S_1 and S_0 ,



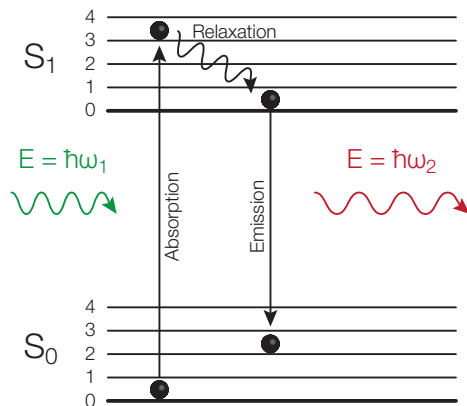


Fig. 3.1: A Jablonski diagram of fluorescence. The process starts with excitation of one electron in the fluorophore to the excited state, S_1 , by absorption of one photon. A loss of energy due to vibrational relaxation follows, then de-excitation by photon emission to the ground level, S_0 .

The result is that the wavelength of the emission photon is longer (lower energy) than the wavelength of the excitation photon, $\omega_2 < \omega_1$.

The discrepancy between the excitation wavelength and the emission wavelength can be utilized for imaging purposes. Since only the emission wavelength carries fluorescent information, all other wavelengths can be filtered out. The emission light originates from the labeled molecules of interest so the emission light carries a diffraction limited map of where the molecules of interest reside and can be captured by a camera.

Total internal reflection fluorescence microscopy

As previously described, the subject of interest is presented on a flat support with the region of interest being within a small distance perpendicular to the surface. To take advantage of this, an often used method for imaging SLBs is so called total internal reflection fluorescence microscopy (TIRF).^[5;63–65]

In a TIRF setup, the sample is illuminated at an angle of incidence, θ_i , larger than the critical angle, θ_c , Fig. 3.2(a), achieving total reflection at the solid-fluid interface of the sample.^[66] Total internal reflection gives rise to a non-radiative evanescent wave propagating along the boundary surface.^[5] This evanescent field is subject to exponential decay along the z -axis of the sample and thus only extends a couple of hundred nanometers into the bulk of the sample^[5] making it ideal for imaging fluorophores close to the interface, while fluorophores in the bulk remain dark and invisible.

Quenching and photobleaching

Quenching of fluorophores is an umbrella term describing decreased fluorophore fluorescence and it includes reactions in the excited state (these are primarily reactions with oxygen radicals), energy transfer, collisions and complex formation. It is impor-

tant to note that quenching is not due to the fluorophore not getting excited, but rather that excited electron takes a non-radiative path back to the ground state.

Energy transfer is a quenching process where the energy of the excited state photon is transferred to another molecule. This molecule can for instance be another fluorophore or a metal in the vicinity of the excited fluorophore. Gold, as used in the barriers in paper I and nanoparticles in papers III and IV, is a particularly efficient fluorescence quencher. If a fluorophore is within approximately 10 nm of a gold nanoparticle or gold film its fluorescence intensity will be greatly decreased.^[67;68] Energy transfer between two fluorophores is called Förster resonance energy transfer (FRET) and depends on one over the distance between the fluorophores to the power of six. The heavy dependence on the distance between the fluorophores means that FRET can be used as a tool for measuring nanoscopic distances between molecules, an important tool when studying for instance ligand-receptor pairs.^[64] Fluorophores can also self-quench, something that primarily happens at very high fluorophore concentrations. Self-quenching has been utilized to study for instance swelling of vesicles when subject to an osmotic shock.^[69]

The fluorescence intensity can also decrease due to a transition into a triplet state. This, much like fluorescence in it self is a quantum process. The transition between the singlet state S_1 and the triplet state T_1 is a so called forbidden transition. The term forbidden is used rather lightly, but refers to the fact that this relaxation is not the most energy efficient and therefore relatively unlikely rather than forbidden. Relatively unlikely means that while this relaxation will not be the most frequently occurring. However, since the fluorophore is excited thousands of times every second, the forbidden transition will sometimes happen. Since relaxation to the ground state, S_0 , also requires a forbidden transition, the electron in the triplet state will reside in there for some time and eventually de-excite by emitting a photon in what is known a phosphorescence.^[70] In equivalence to Eqs. (3.1) and (3.2), phosphorescence can be explained using an equation,



The main difference between fluorescence and phosphorescence is one of time scales. While the de-excitation in fluorescence happens at a nanosecond scale, the time scale for phosphorescence is, depending on the molecule in question, somewhere in the range between milliseconds to minutes and even hours.^[70] During the time the fluorophore is trapped in the triplet state it can not be excited by an incoming photon and therefore, can not de-excite by photon emission in fluorescence. Hence, the fluorophore is dark.

Additionally, every single fluorophore can only be excited a finite number of times before the molecule is destroyed and impossible to excite further. The number of excitations can be further reduced by reactions in the excited state.^[70] The latter of these two processes, transition into a triplet state and destruction of the fluorophore are generally referred to as photobleaching and has to be accounted for when working with fluorophores. To an extent this can be done by using photostable fluorophores with a high quantum yield.*

*The quantum yield of a fluorophore is the number of emitted photons per absorbed photon.

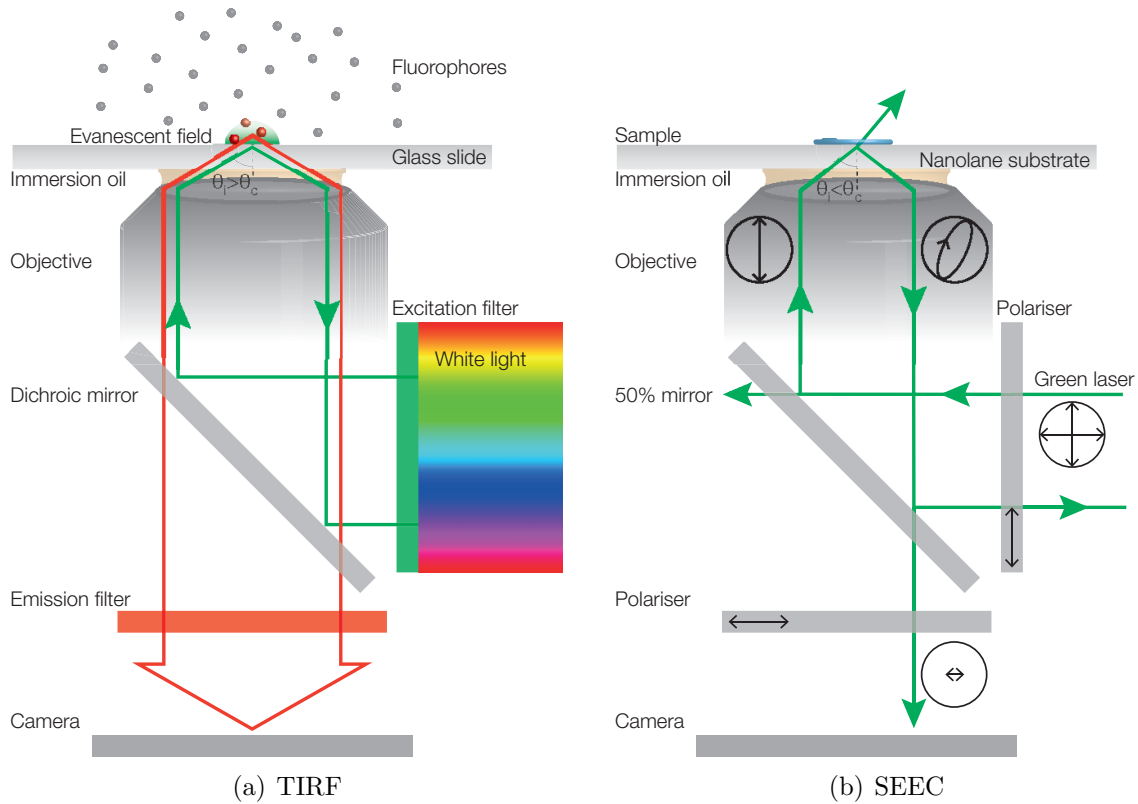


Fig. 3.2: Schematic illustrations of the microscopy setups. (a) The TIRF setup; a white light source is used with the light passing through a crescent shaped aperture to fulfill total reflection at the sample. A filter cube, specific for the fluorophore used, consisting of an excitation filter, a dichroic mirror and an emission filter is present to select the appropriate wavelengths and direct those to the sample and the camera respectively. (b) The SEEC setup; a green laser passes through a polarizer and is directed towards the sample at an angle of $\sim 30^\circ$ by a 50% mirror. The polarized light then hits the sample resting on the anti-reflecting ellipsometry substrate. The sample changes the polarisation of the light in the reflected beam which passes a polarizer that is orthogonal to the first one on its way towards the camera.

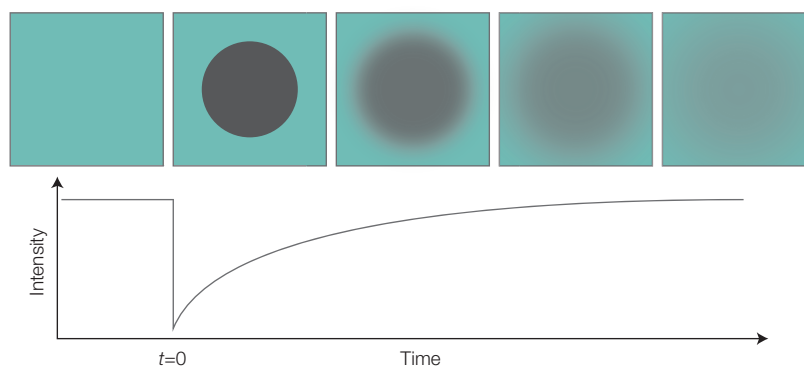


Fig. 3.3: Schematic illustration of a FRAP experiment. At $t = 0$, a circular area is illuminated by a focused strong light source. This exposure bleaches all fluorophores within the illuminated area. The recovery of fluorescence as the bleached fluorophores diffuse out of, and non-bleached fluorophores diffuse in to, the area is then monitored with respect to time. The recovery can be related to the diffusivity of the labeled species.

Fluorescence recovery after photobleaching

While photobleaching can be troublesome when performing time-lapse recordings of fluorophores, it needs not be solely bad. Instead, the limited lifetime of a fluorophore can be utilized. One commonly used technique for measuring diffusivity is FRAP^[71–73] as used in paper II. In FRAP a small area of the sample is illuminated using a very bright light source, thus destroying all the fluorophores in that area and creating a black spot surrounded by active fluorophores, see Fig. 3.3. Diffusion will cause some of the bleached fluorophores out of the black spot and some of the active fluorophores into the black spot and eventually result in a homogenous intensity across the sample. This diffusion process can be monitored using time-lapse recording and the time to reach a homogenous sample, the fluorescence recovery, is indicative of the diffusivity of the sample.^[73–77]

3.1.2 Label-free microscopy techniques

While fluorophores are impressive as a means of visualization in their own right, modifying biological molecules with an often hydrophobic molecule, like a fluorescent dye, has its drawbacks, and may introduce additional interactions between the molecule of interest and its surroundings, which in turn can introduce false positives in assays where the molecule of interest is studied. Studies where these non-specific interactions are eliminated are therefore of interest, and the most efficient way of reducing these non-specific interactions are to simply eliminating the need of labelling.

Surface enhanced ellipsometric contrast

SEEC has during this thesis work been used for visualization of a protein film (paper II), as well as gold nanoparticles (papers III and IV) on top of an SLB. The major difference between this setup and the fluorescence microscope is the sample substrate,

constituting multiple $\lambda/4$ -layers of dielectrics with different refractive indices. The refractive index and thickness of each layer is chosen such that the polarization of light is unchanged upon reflection on the sample. Utilizing orthogonal polarizers in the light path, situated before and after reflection on the surface respectively, this leads to the surface being anti-reflecting.^[78;79] However, on changing the refractive index of the medium above the surface, for example by adsorption of a thin film such as an SLB, the polarization of the reflected light will change and bring information about the adsorbed thin film, see Fig. 3.2(b) for a schematic illustration of this process. SEEC, while being a relatively new technique, has for instance been used to visualize gold nanoparticles, self-assembled monolayers^[80] and lipid domains within a heterogenous SLB.^[81]

SEEC is sensitive to the effective refractive index of the medium directly above the surface of the substrate. Given a medium with a refractive index above that of water ($n > 1.33$, true for biological material) a thicker or denser layer yields a higher effective refractive index, as long as the thinner layer does not occupy the entire sensing volume of the substrate. In paper II accumulation of peripheral membrane proteins bound to an SLB was studied using the fact that the effective refractive index increased as the proteins were accumulated in the hydrodynamic trap. One disadvantage of the technique is that the same change of effective refractive index could be the result of either an increase in thickness or density of a layer, with no good method of realizing which it is.

In papers III and IV, SEEC was used to visualize gold nanoparticles on a supported membrane. While the refractive index sensing capabilities of an SEEC substrate were relied upon in paper II, it is not crucial for visualizing gold nanoparticles in the size range used in papers III and IV. In fact, these gold nanoparticles can be visualized using the setup shown in Fig. 3.2(b) with a regular microscopy slide in place of the SEEC substrate, with the only penalty being a lower sensitivity meaning that larger gold nanoparticles, yielding a larger signal, must be used.

That the gold nanoparticles are visible in this setup, regardless of the substrate, is an effect of plasmonic properties of the gold nanoparticles. Briefly; the gold nanoparticles, like metals in general, can to the lowest order be approximated as an electron gas with free conduction electrons moving through a fixed positive background, consisting of nuclei and core electrons. Electromagnetic radiation incident on a metal surface can couple with the electron cloud and excite a so called surface plasmon polariton. A nanoparticle however, is too small to accommodate a surface plasmon polariton and instead incident electromagnetic radiation can couple with the free electron cloud into a localized surface plasmon, a collective oscillation of all the free electrons in the nanoparticle. The efficiency of the interaction between the photon and the free electron cloud depends on the wavelength of the electromagnetic radiation and the material (more specifically the dielectric function), the size and the shape of the nanoparticle. Hence, every nanoparticle will have an interaction maximum at some wavelength, the so called localized surface plasmon resonance, at which the particles interaction cross-section is the largest. The wavelength of this maximum can be calculated using Mie theory,^[82;83] and for gold nanoparticles there is a maximum at $\lambda \approx 550$ nm, at which the nanoparticles will scatter, but also absorb, the most light.

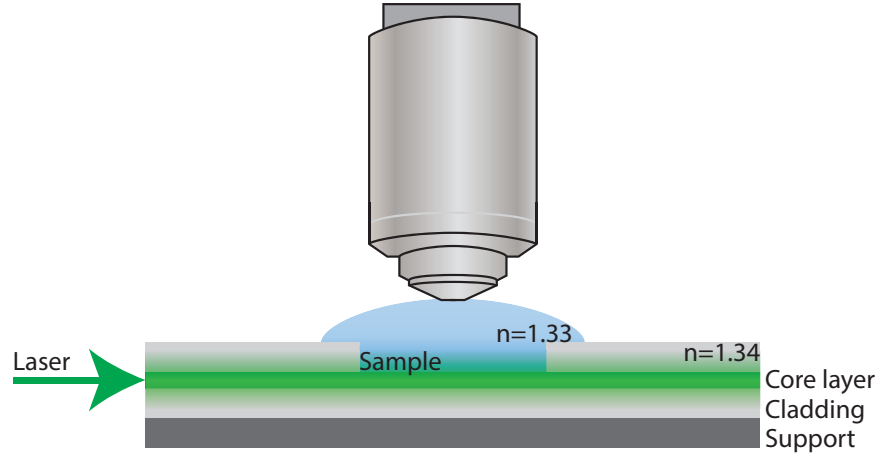


Fig. 3.4: Schematic illustration of Evanescent Wave Scattering Microscopy. An optical wave guide is manufactured on a Si wafer support. The wave guide consist a core layer, made from spin on glass, covered on both sides by a cladding layer. A measurement well is cut into the upper cladding layer, exposing an area of the core layer. Light propagating through the wave guide gives rise to an evanescent field in the cladding layer and also in the measurement well, where it can be used to either excite fluorophores (similar to TIRF) or scatter off of nanoparticles. Some of the emitted or scattered light propagates through the objective and is captured on a camera.

This wavelength is quite close to the wavelength of the light source in the SEEC setup, $\lambda = 525 \text{ nm}$. Thus, the gold nanoparticles are visualized by virtue of scattered light, with the SEEC setup where the sample is located between crossed polarizers serves to eliminate the background.

Evanescent wave scattering microscopy

Due to the high sensitivity with regards to visualizing gold nanoparticles, evanescent wave scattering (EWS) microscopy was used for part of the study presented in paper III. The basis for EWS is a planar waveguide with a laser coupled to one of the facets of the wave guide. The waveguide used in this thesis work was made from three layers spin coated onto a silicon wafer support, see Fig. 3.4, with a core layer made from spin on glass encased on either side by a cladding layer made from the polymer CYTOP. Coupling of laser light into the waveguide yields a propagating electromagnetic field through the core layer, with an evanescent field extending into the cladding layer, due to total internal reflection between the core and cladding layers, much like an evanescent field is created in TIRF and similarly this evanescent field can be used to excite fluorophores if they are within reach of the field, or scatter off of nanoparticles. A measurement well is therefore etched through the upper cladding layer down to the core layer. To not cause scattering and refraction of light at the edges of the well, it is crucial that the cladding layer has a refractive index close to that of an aqueous solution, which is the reason for CYTOP, a polymer with a refractive index of $n = 1.34$ was used.

In comparison to the SEEC-based gold nanoparticle visualization discussed pre-

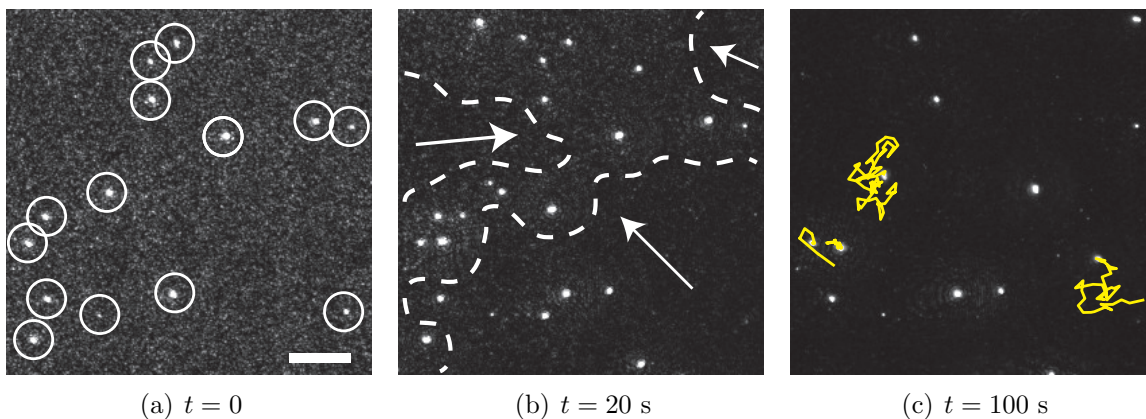


Fig. 3.5: Time lapse of gold nanoparticle-NMV construct rupturing on a spin on glass surface. In (a) the brighter dots correspond to a gold nanoparticle on the surface, indicated by a surrounding white circle. The dimmer dots correspond to vesicles adsorbed to the surface. (b) After 20 s a rupturing wave can be seen propagating through the field of view, indicated by a dashed white line. The presence of membrane material on the surface retards the rupture, particularly in the presence of a gold nanoparticle. (c) At $t = 100$ s the vesicle rupture is almost complete, as indicated by the diffusing gold nanoparticles. The scale bar, shown in (a), is $10\ \mu\text{m}$.

viously, EWS has an advantage in sensitivity partly due to the significantly lower background intensity, a result of the optical setup with the laser perpendicular to the optical axis of the microscope ensuring that no light reaches the camera in the absence of material on the waveguide. The higher sensitivity enables visualization of smaller nanoparticles than what is possible in the SEEC-based setup, and even of single non-labeled SUVs on the surface.^[84] Due to this higher sensitivity EWS used as a control for visualizing the rupture of pre-incubated gold nanoparticle-NMV constructs into a supported membrane, see Fig. 3.5. While the sensitivity beats that of the SEEC-based setup, EWS is currently not compatible with microfluidics, due to a lack of compatibility with inverted microscopes.

3.1.3 Acquisition and resolution

While pen and paper was used to draw what the observer saw in the ocular in the childhood of the optical microscope, cameras are used to capture the processes occurring on the microscope today. Thus, to fully understand implications of what can be observed using a microscope knowledge of key characteristics of a camera is necessary. In a time when almost every cell phone comes with a camera, certain of these characteristics, such as spatial resolution, are common knowledge, but their implications on the images produced in the specific setting that is a microscope, are not.

Briefly; a camera is a device that captures light, producing an image. In a digital camera, light is captured by pixels, light sensitive elements that produce a voltage corresponding to the intensity of light impinging on the pixel during the exposure. Several (up to several millions) of these pixels constitute the sensor, and the sensor

is what captures what we call the image. The voltages read from the sensor after exposure are converted into a number by a signal processor and these values are, together with the spatial information the sensor provides, saved as the image file.

Starting with spatial resolution, from the brief description above it is obvious that the larger the number of pixels on the sensor, the better the spatial resolution of the produced image will be and thus the smaller the features that can be seen in the image. The number of pixels on the sensor can be increased in two ways, i) by decreasing the size of the pixels or ii) by increasing the size of the sensor. The former of these methods has the inherent drawback that decreasing the size of the pixel inevitably means that it will capture less light, which pushes the pixel closer to the noise floor. Noise is introduced when reading the pixel voltage and for the purposes of this discussion it can be regarded as a per read event only number, To an extent the decrease in photons per pixel can be counteracted by either increasing the illumination intensity, but this has the drawback that the sample might be damaged by the higher irradiation or increasing the exposure time.

The exposure time, or integration time, is the time during which the sensor captures incident light. The fact that the exposure time is non-zero means that any moving object will have a displacement during the exposure time, meaning that absolute sharpness is impossible. The resulting blur is called motion blur and increasing the exposure time also increases the motion blur, since the displacement of moving particles will be larger. A longer exposure time also puts a limit to the rate at which images can be acquired, decreasing the accuracy with which a moving object can be tracked, something that will be discussed in section 4 of this chapter.

Thus, it may seem like the latter of the two methods for increasing spatial resolution is the better, and generally it is. However, a larger sensor results in larger optical elements, yielding a bulkier and more expensive microscope (this relates to the size difference between the camera in a cell phone and a dedicated camera), in addition to the increased manufacturing difficulty and costs for the larger sensor.

The usefulness of high spatial resolution in the realm of microscopy can however be challenged on basis of matters less mundane than money. In 1873 Ernst Abbe coined the resolution limit; stating the minimum distance two objects must be separated in order to resolve them as discrete objects. At separations smaller than the resolution limit, the point spread function of the two objects overlap to such an extent that they become indistinguishable. Formally, the (Rayleigh) resolution limit is known as $d = \frac{1.22 \lambda}{2 \text{NA}}$, where NA is the numerical aperture of the objective. The numerical aperture, coincidentally also coined by Abbe, is a dimensionless number that describes the size of the light cone that can enter *e.g.* an objective.^[66] With wavelengths of visible light being in the range of $\sim 400 - 750$ nm the resolution limit for optical microscopy is ~ 200 nm. If two particles can not be distinguished from each other if they are separated by d , it makes no sense to have a microscope equipped with a camera that yields a higher spatial resolution than d .

The resolution limit does, however, not have any effect of the precision with which the position of an object can be determined. The key to determining the position of the object is that the point spread function of a small spherical object is a Gaussian function. Hence, fitting the point spread function of the object, recorded with the

cameras resolution, with a Gaussian function gives the particles position with an accuracy far higher than that of the camera.

3.2 *Microfluidics and hydrodynamic forces*

Microfluidics, as the name implies, is a research area where relatively small volumes of liquid are put through structures with small, μm , dimensions.

The advantage of using microfluidics is that the sample consumption is lower than it would have been had the dimensions not been in the micrometer range and that the flows that are created are laminar, as characterized by low Reynolds numbers, meaning that they are easily characterized. In all papers appended to this thesis, microfluidics has facilitated the work performed. In this section is presented an introduction to the aspects of microfluidics that have been crucial for the work presented.

Perhaps the main pillar of the experimental work has been the utilization of hydrodynamic drag forces to induce lateral movement in an SLB and, more importantly, of molecules protruding from the SLB. The drag forces have been applied using a liquid flow above the SLB using two different techniques. In papers I, III and IV, the hydrodynamic drag forces were applied using liquid flow within a microfluidic channel cast in the polymer polydimethylsiloxane (PDMS) by the method of replica molding,^[85;86] while in paper II the hydrodynamic drag was applied locally using a micropipette positioned in close proximity above the SLB.^[87]

3.2.1 *Shear-driven lipid bilayers*

In papers I, III and IV microfluidic channels were molded from PDMS in the shape of a cross with four access points, see Fig. 3.6. In papers I and III, a membrane edge was introduced, using the opposed access points as inlets (1 and 4) and outlets (2 and 3) respectively and injecting lipid vesicles into access point 1 while injecting buffer into access point 4, resulting in a supported membrane covering only half the channel, see Fig. 3.7. When the SLB is formed, valves at the outlets are closed and the inlet at access point 4 is converted to an outlet. A buffer solution is then flowed through the channel at a high flow rate. Due to the flow being applied through the channel, a hydrodynamic force is exerted on all of the SLB in arm 1 of the channel. Remember that the SLB, as explained in chapter 2, essentially is a two-dimensional fluid consisting of two leaflets of lipids that can move independently. Due to the hydrodynamic flow profile in the channel, more of which will be explained later in this section, the upper leaflet will experience a larger force than the lower, and will start to slide on the lower leaflet, resulting in a forward motion not unlike that of a caterpillar band, see Figs. 3.8 and 3.9 for a schematic illustration and an optical micrograph time lapse recording of a shear-driven SLB respectively.

The schematic illustration shown in Fig. 3.8 displays the force balance in the bilayer, where σ_{hydro} is the hydrodynamic shear force, b is the intermonolayer frictional coefficient, b_{ls} is the frictional constant between the lower leaflet and the support. v_{u} , v_{l} and v_{f} are the velocities of the upper and lower monolayer and the bilayer front respectively. Under idealized, no-slip conditions, Figure 3.8 gives the following

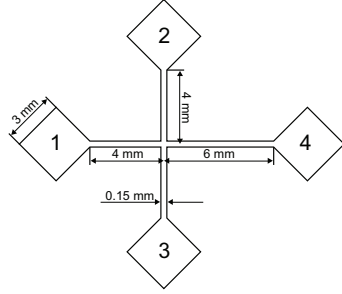


Fig. 3.6: The 4-arm microfluidic channel design as seen from above.

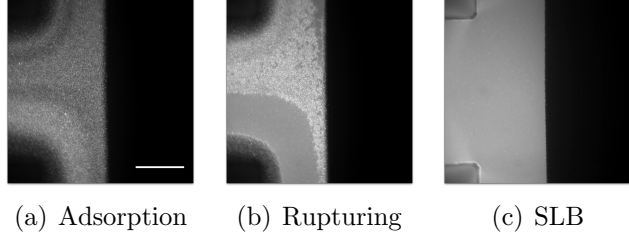


Fig. 3.7: Fluorescence time lapse of the formation of an SLB by injection of a lipid vesicle solution from the left, attachment point 1 as seen in Fig. 3.6. Compare to Fig. 2.3. The scale bar is $50 \mu\text{m}$.

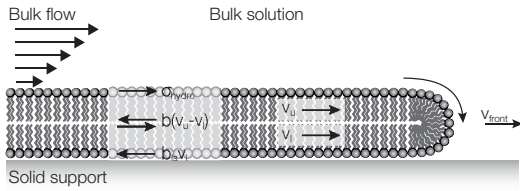


Fig. 3.8: Schematic illustration of a rolling bilayer.

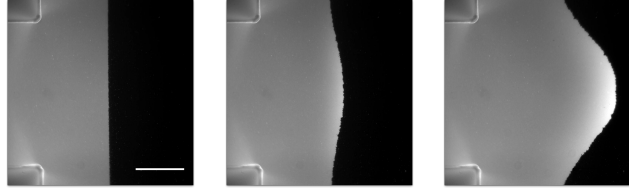


Fig. 3.9: Fluorescence time lapse of a shear-driven SLB with a hydrodynamic force applied via buffer flow above the SLB from the left. The scale bar is $50 \mu\text{m}$.

expressions for the velocities of the upper and lower monolayers^[88]

$$v_u = \sigma_{\text{hydro}} \left(\frac{1}{b} + \frac{1}{b_{\text{ls}}} \right) \quad (3.4)$$

$$v_l = \frac{\sigma_{\text{hydro}}}{b_{\text{ls}}}. \quad (3.5)$$

Assuming no-slip conditions, this dictates that the velocity of a fluid relative to the surface should be zero at the fluid-surface boundary, the bulk flow velocity will be larger in the center of the channel than at the walls, floor and ceiling.^[89] This means that the hydrodynamic shear-force will be larger, and thus that the velocity of the monolayers will differ across the width of the channel. Furthermore, it also leads to the upper monolayer experiencing a larger force than the lower.

The average velocity of the advancing bilayer front can be determined as^[90]

$$v_f \approx \frac{\langle v_u \rangle + \langle v_l \rangle}{2}, \quad (3.6)$$

where $\langle v_u \rangle$ and $\langle v_l \rangle$ describes the average velocity of the upper and lower monolayer across the width of the channel respectively. Jönsson et al.^[90] has shown that, in fact,

the lower monolayer is almost stationary, corresponding to

$$v_u \approx \frac{\sigma_{\text{hydro}}}{b} \quad (3.7a)$$

and

$$v_f \approx \frac{v_u}{2}. \quad (3.7b)$$

The variations in the velocity of the SLB across the width of the channel has in previous work for instance decreased the efficiency of separation of membrane-bound proteins^[91] due to overlap between the separated populations close to the channel walls. During this thesis work, a way to circumvent this limitation has been investigated by inclusion of a gold barrier on the floor of the microfluidic channel confining the SLB to the centermost portion of the channel where the variation in the hydrodynamic shear force is almost zero.

The gold barriers were fabricated using photolithography, see Fig. 3.10, during which the glass slide that will later constitute the channel floor was spin coated with a positive photoresist. In the next step, the photoresist was exposed with UV light allowing the exposed photoresist to be removed from the slide when submerged in photoresist developer. Gold was then evaporated onto the photoresist-patterned glass slide. The surplus gold was removed by submersion of the slide in a lift-off solution, dissolving the remaining photoresist. The PDMS channel structure was then bonded to the finished channel floor using oxygen plasma treatment^[90] to form the finished channel.

The resulting microfluidic device was used in paper I to accumulate, see Fig. 3.11(a), and separate, see Fig. 3.11(b), peripheral membrane proteins based on their membrane friction, with the resulting proteins residing in spatially separated and, crucially, confined regions of an SLB. In papers III and IV similar microfluidic devices were used to apply a flow pressure yielding a force acting on nanoparticles bound to an SLB on the floor of the device, discussed more in depth in the next section.

3.2.2 Hydrodynamic kiting

The force acting on an object exposed to a hydrodynamic flow can be written as:

$$F_{\text{hydro}} = A_{\text{hydro}}\sigma_{\text{hydro}}, \quad (3.8)$$

where A_{hydro} is the cross sectional area exposed to the bulk flow.^[92] A quick look at eq. 3.8 validates what is intuitively clear; the hydrodynamic force acting on an object increases with the hydrodynamic shear force, which scales with the flow velocity, and with the cross sectional area of the object.

Increasing the flow speed would hence have the same effect on the velocity of an object as increasing its cross sectional area. The difference would be the influence these changes would have on the environment of the object. In the first case, all objects in the surroundings would be similarly affected by increase in hydrodynamic force acton on them and would thus move faster along the flow direction. In the second case, however, only the object with the increased cross sectional area would

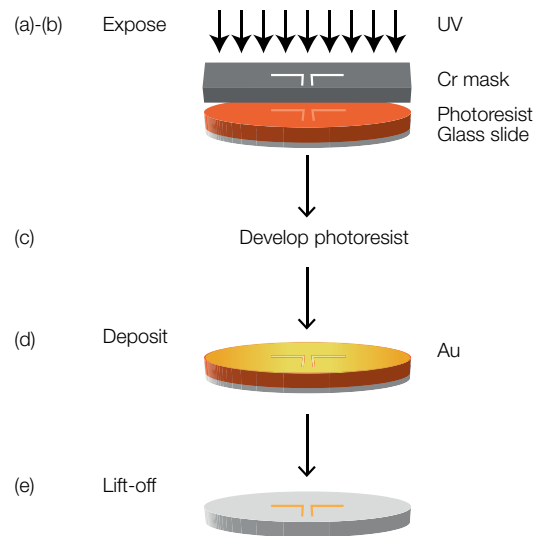


Fig. 3.10: Schematic illustration of the fabrication of the gold barrier. First a glass substrate is spin coated with positive photoresist (a). The photoresist is exposed to UV-light through a chromium mask with the structure that will be transferred to the substrate (b). The exposed photoresist is removed using a developer (c). Gold is then evaporated onto the substrate (d) and then the remaining photoresist is removed together with the surplus gold (e). The result is a gold structure from the chromium mask on the glass substrate.

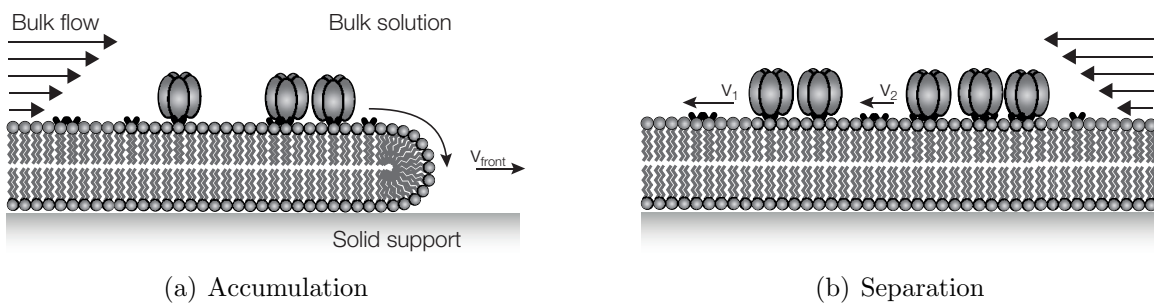


Fig. 3.11: (a) A shear-driven SLB with a bulk flow from left to right in the figure, resulting in an accumulation at the front of the SLB. (b) When reversing the flow the accumulated species are separated based on, in the case of CTB bound to G_{M1} , the number of anchoring points.

be influenced by the larger force, leaving all objects in its surrounding unaffected. Thus, by selectively enlarging the cross-sectional area of one pre-selected membrane component would make it possible to manipulate the position of this component in the membrane while not significantly affecting the random movement of the molecules in the surrounding membrane.

This insight offers a potential solution to a problem that's been hampering the study of membrane components; how to locally enrich a membrane component in a membrane environment consisting of multiple molecular components. As explained in chapter 2, the cell membrane is composed of amphiphilic molecules in a bilayer structure and thus, all molecules integral to the membrane inherit this amphiphilicity. Membrane proteins, essentially a folded string of amino acids whose function depend as much on the amino acids as on the structure into which they fold, are thus sensitive to their surroundings and if they are pulled out of the membrane in which they naturally reside into an aqueous environment, they will refold or unfold and loose their structure. Unfortunately this means that the well developed methods used to enrich water soluble proteins can not be used on membrane proteins. The most common way of overcoming this obstacle is to make the membrane proteins water soluble, by dissolving them in a detergent, and then treat the protein as if it was water soluble, using the same methods and protocols. While this approach generally works rather well, it has some distinct disadvantages. The most obvious is the need to get rid of the detergent when the protein is reconstituted back into its natural lipid bilayer environment, often a requirement to study their function and other properties. A slightly less obvious disadvantage is that any other molecule, either in the membrane or on its interior/exterior, associated to the protein in the native environment risks being lost upon detergent solubilization.

One way to circumvent the limitations put in place by treating membrane proteins as if they were water soluble, is to enrich membrane proteins while they reside in their natural environment, the cell membrane. Prior attempts at in-membrane enrichment of membrane proteins or membrane-associated proteins, using electrophoresis,^[37;93-95] in conjunction with nano-lithography defined surfaces^[96;97] and electroosmosis,^[98] surface acoustic waves,^[99;100] continuous extraction^[101], nanopatterned bilayers^[102] and hydrodynamic forces^[90;91;103] have, while successful in their own right, all have had issues with the specificity of the enrichment due to the force driving the enrichment acting similarly on all molecules in the membrane with a similar, in the case of electrophoresis, charge or, in the case of hydrodynamics, protrusion size. Hence, while enrichment of membrane molecules is possible using these techniques, the enrichment will not be of a single species, especially if the starting material is something complex like a cell membrane. Instead a larger number of molecules will be enriched in certain regions while others will be depleted.

Falling back onto what was discussed previously about increasing the cross-sectional area of a membrane component, the question is how to i) increase the cross-sectional area of an object in the membrane and ii) how to make it selectively targeting certain pre-determined entities in the membrane. To overcome the first challenge, nanoparticles were conjugated to the membrane entity, thus artificially increasing the size of the protruding domain of a membrane protein by two to three orders of magnitude,

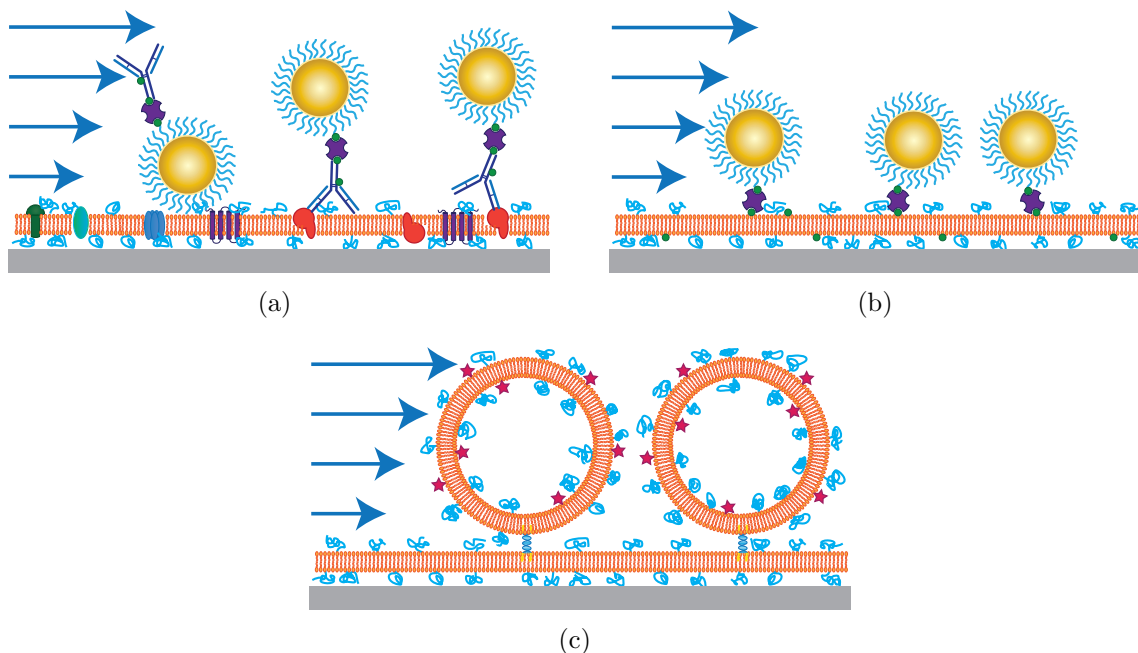


Fig. 3.12: Schematic illustration of the concept of hydrodynamic kiting. Two types of nanoparticles, one inorganic gold nanoparticle (a) and (b) and one organic, a lipid vesicle (c), linked to an SLB using three different linkers. In (a) gold nanoparticles are specifically linked to a pre-selected membrane proteins via a biotinylated antibody. In (b) gold nanoparticles are specifically linked to biotin in the SLB using SA. In (c) lipid vesicles are linked to an SLB using cholesterol-anchored double-stranded DNA.

as schematically illustrated in Fig. 3.12(a). To make it specific, the conjugation of nanoparticles was done using antibodies. The use of antibodies makes the method quite versatile, since the only thing required for the method to work with a certain target is that a reasonably high affinity monoclonal antibody targeting the ectodomain of the target exists. The synthesis and functionalization of the gold nanoparticles is covered in chapter 3.3.

Antibody-modified gold nanoparticles, see Fig. 3.12(a), were not the only nanoparticles that were used as nanoparticle kites in this thesis work, however. Gold nanoparticles with streptavidin were also bound directly to biotinylated lipids in the supported membrane, see Fig. 3.12(b), and liposomes were linked to a supported membrane using cholesterol anchored double-stranded DNA, see Fig. 3.12(c). Applying a hydrodynamic force to the kites, as indicated in Fig. 3.12 yields movement of the nanoparticles along the flow direction, see Fig. 3.13, where three gold nanoparticles linked to a supported membrane starts to move along the flow direction upon application of a weak bulk flow from left to right. The bulk flow strength in this case is $10 \mu\text{L}/\text{min}$ in a microfluidic device with a cross section of $150 \times 110 \mu\text{m}^2$ (width \times height), corresponding to an average velocity in the channel of $\sim 1 \text{ cm}/\text{s}$, exerting a force of 16 fN on the $\varnothing = 50 \text{ nm}$ gold nanoparticles.

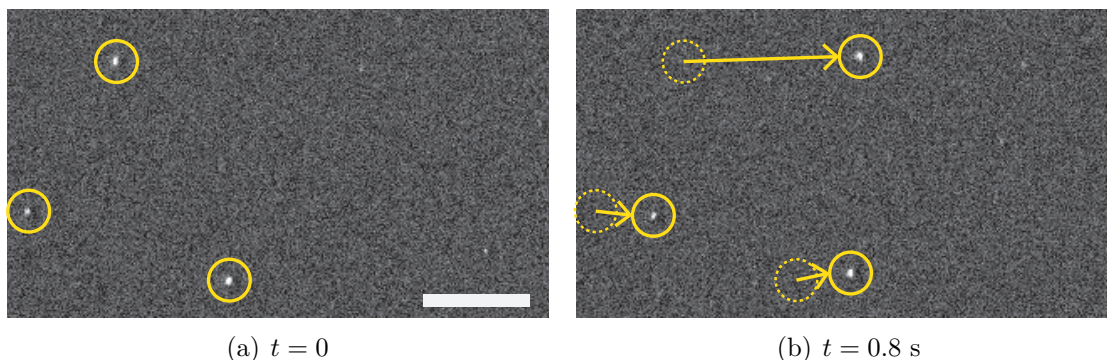


Fig. 3.13: Applying a gentle hydrodynamic force from the left in the figure yields movement of the gold nanoparticles from left to right as illustrated by this time lapse. The scale bar is $10\ \mu\text{m}$.

3.2.3 Hydrodynamic trapping

For the hydrodynamic trapping experiments in paper II, a SEEC sample substrate was glued to the bottom of a drilled through Petri dish, creating a second, smaller Petri dish with a volume of $\sim 10\ \mu\text{L}$, see Fig. 3.14. An SLB was formed on the substrate by exposure to a lipid vesicle containing suspension for 30 minutes after which peripheral membrane proteins were bound to the SLB using the same approach. The comparably longer time for SLB formation in comparison to the microfluidic channel is due to the reduced effectiveness of the transport of vesicles to the surface which is in turn due to the absence of flow.

A glass micropipette with a tip radius of $\sim 1\ \mu\text{m}$, see Fig. 3.15, was positioned 1-5 tip radii from the SLB using a piezo controlled stage. Figure 3.14 shows a schematic illustration of the experimental setup. The distance was monitored by measuring the current between an electrode inside the pipette and a reference electrode in the solution. A current drop of $1 - 2\%$ corresponds to approximately 1 tip radius in distance between the pipette and the SLB.^[87]

With the micropipette in position a hydrodynamic force could be applied to the SLB by applying either a negative or positive pressure to the pipette, thus causing a bulk flow into and out of the pipette respectively. Much like in the microfluidic channel, the applied bulk flow yields a hydrodynamic force that acts on the SLB and the peripheral membrane proteins bound to the SLB. Since the hydrodynamic force decays rapidly with the distance from the tip, the effect is much more localized than in the microfluidic channel. The effect of an applied negative pressure is an accumulation of the peripheral membrane proteins underneath the micropipette, *i.e.* hydrodynamic trap, see Fig. 3.16(a), whereas an applied positive pressure creates a cleaned-out area below the tip, see Fig. 3.16(b). Applying a sufficiently large positive pressure creates a hole in the SLB, exposing the surface to the bulk solution, data not shown.

By first turning on the hydrodynamic trap to accumulate proteins and subsequently turning off the trap, letting the proteins diffuse back to the equilibrium cov-

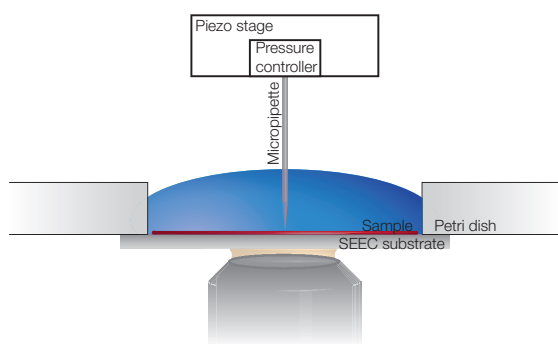


Fig. 3.14: Schematic illustration of the hydrodynamic trap setup.

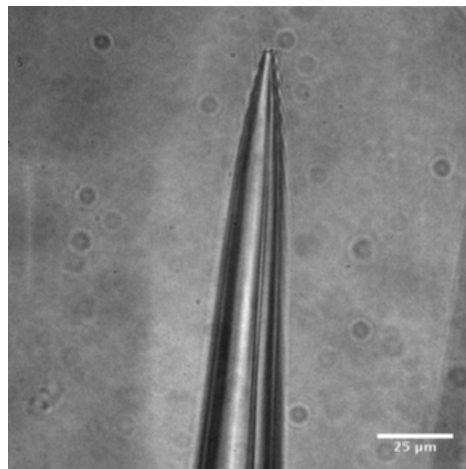


Fig. 3.15: An optical micrograph of the micropipette. The scalebar is 25 μm.

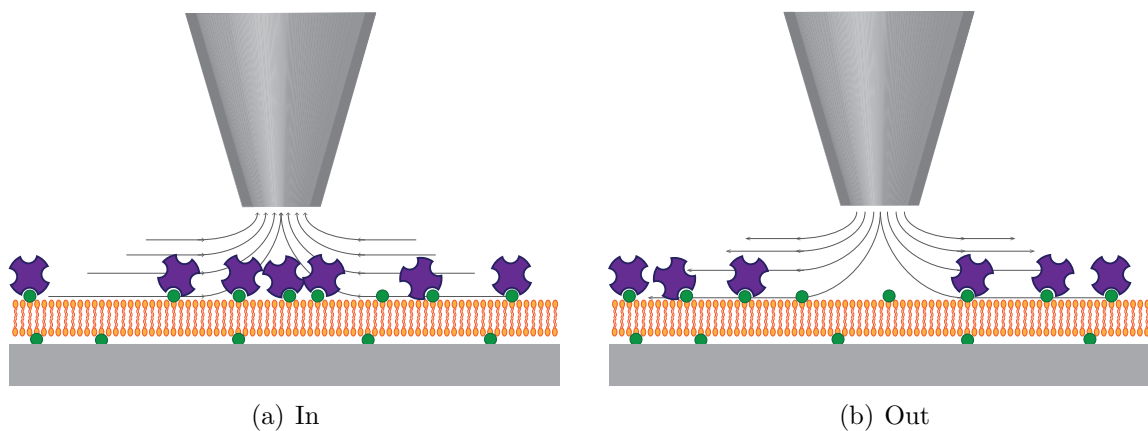


Fig. 3.16: Schematic illustrations of the hydrodynamic trap when applying (a) negative and (b) positive pressures through the pipette. In (a) the molecules bound to the SLB are accumulated underneath the tip whereas the area directly underneath the tip is cleaned from molecules in (b). Applying a larger positive pressure would also push the SLB away.

erage, allows diffusivity measurements of the proteins.^[87] Since the system was setup such that an increase in the optical thickness yields a decrease in the intensity signal, the data are so similar to FRAP data that the same mathematical analysis as used in FRAP can be carried out on the SEEC data.

The accumulation underneath the pipette tip was fitted to a Gaussian function

$$I_r(r,t) = I_0 \left(1 - K e^{-r^2/w^2} \right), \quad (3.9)$$

where w is the width of the Gaussian. The decrease in protein density and thus the increase in signal with time was fitted to the expression^[104]

$$I(t) = \alpha \left(1 - \frac{w^2}{R^2} K \left(1 - e^{-\frac{R^2}{w^2 + 4Dt}} \right) \right), \quad (3.10)$$

where $R = w/\sqrt{2}$ is the radius of the accumulation spot and α , K and the diffusivity, D , are parameters that are to be fitted.

The advantage of the use of the SEEC substrate is that diffusivity measurements could be carried out on both labeled and non-labeled molecules under the same circumstances, more of which will be discussed in chapter 4.

3.3 *Synthesis and functionalization of gold nanoparticles*

In paper III and IV, gold nanoparticles were used to increase the hydrodynamic force acting on a selected species from the bulk flow. The gold nanoparticle, relatively large in comparison to the membrane components it was targeting, increase the effective cross section of the selected species that is exposed to the bulk flow, thereby increasing the force acting on the species. In theory, this means that an applied bulk flow can be kept at a sufficiently low level so that only the selected species is influenced by the flow, starting to move along the flow, while the motion of other membrane components is not significantly influenced.

While the hydrodynamic kites could have been made of many different materials, due to the relative ease of synthesis and the existence of well-developed thiol-chemistry, gold nanoparticles were chosen as force mediators. Another advantage of the gold nanoparticles is that they are easily visible using SEEC, phase contrast microscopy and evanescent wave scattering (EWS) microscopy, evading the need for fluorescent labels while also enabling single particle imaging and in an extension, single particle tracking from which diffusivity measurements can be extracted from the individual membrane components, as discussed in section 4 of this chapter.

Three different microscopy techniques were used for visualization of the gold nanoparticles, EWS, SEEC and SEEC-like setup where the SEEC-substrate has been replaced with a regular glass slide. As discussed in section 1 of this chapter, the different microscopy techniques have different sensitivities, meaning that smaller nanoparticles are visible using EWS than using SEEC. While different sized nanoparticles were used, $\varnothing = 50$ nm was decided as a “standard” size, that was clearly visible using all three microscopy techniques, while not so large as to cause blow-out using EWS.

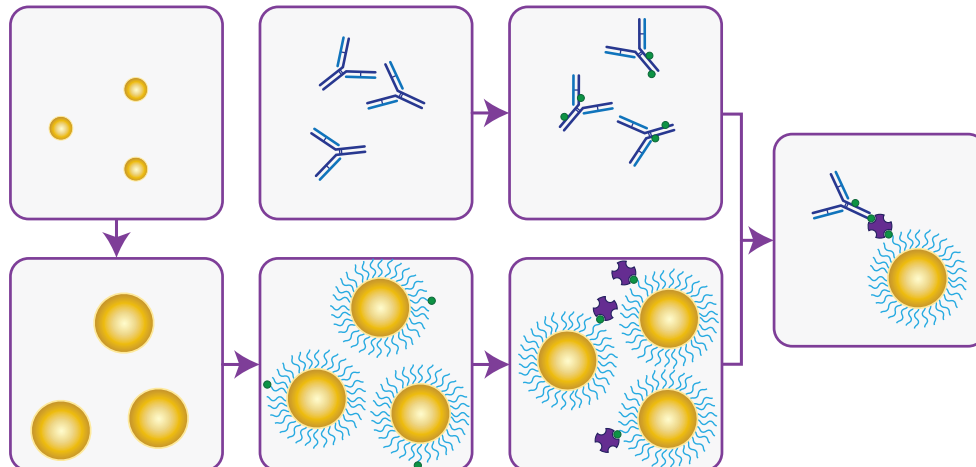


Fig. 3.17: Schematic overview of the gold nanoparticle fabrication process. First a seed solution with $\varnothing \sim 19$ nm is made. In the next stage, larger $\varnothing = 50$ nm gold nanoparticles are grown from the seed particles. These larger particles are then functionalized using a combination of PEG and PEG-biotin with on average one PEG-biotin per gold nanoparticle. Streptavidin is then bound to the gold nanoparticle, to which a biotinylated antibody is bound.

A diameter of $\varnothing = 50$ nm also proved to be a suitable size; linking a particle of that size to the ectodomain of an average membrane protein, with a protrusion cross section of no more than a few nm^2 , would increase the force acting on the membrane protein several orders of magnitude.

The gold nanoparticles were synthesized according to a modified version of the protocol presented by Park *et al.*^[105;106] (see Fig. 3.17 for a schematic overview of the steps involved), whereby first a seed solution of ~ 19 nm gold nanoparticles was prepared by boiling 195 mL milliQ water, 5 mL of 20 mM gold acid ($\text{HAuCl}_4 \cdot 3 \text{H}_2\text{O}$) and 10 mL of 38.8 mM sodium citrate for 20 minutes. The larger gold nanoparticles were then made by seed-mediated growth of the seed particles. $\varnothing = 50$ nm, as characterized by SEM, gold nanoparticles were the result of adding 30 mL of 5.3 mM ascorbic acid to a mixture of 170 mL milliQ, 15 mL of the seed solution (2.8 nM), 4 mL of 20 mM $\text{HAuCl}_4 \cdot 3 \text{H}_2\text{O}$ and 0.4 mL of 10 mM AgNO_3 at a rate of 600 $\mu\text{L}/\text{min}$.

The first step of functionalizing the naked gold nanoparticles was by mixing them with a solution containing a stoichiometric ratio of SH-PEG-OH, SH-PEG-COOH and SH-PEG-biotin at a 100x excess of PEG. In order to limit multivalent interactions between the gold nanoparticles and the supported membrane, the ratio of PEG-biotin to PEG was on average one biotin per Au-PEG core-shell nanoparticle (corresponding to a ratio of $\sim 1/8000$ PEG-biotin/PEG in the case of a $\varnothing = 50$ nm gold nanoparticle). These Au-PEG-biotin nanoparticles were then further functionalized using SA, utilizing one of the strongest ligand-receptor interactions in nature. To avoid aggregation of the gold nanoparticles, *e.g.* by several nanoparticles binding to the same SA, Au-PEG nanoparticles were slowly added to a SA solution containing a concentration of SA corresponding to a 1000x excess of SA to nanoparticles when the two solutions were mixed. To validate that the protocol worked, the function-

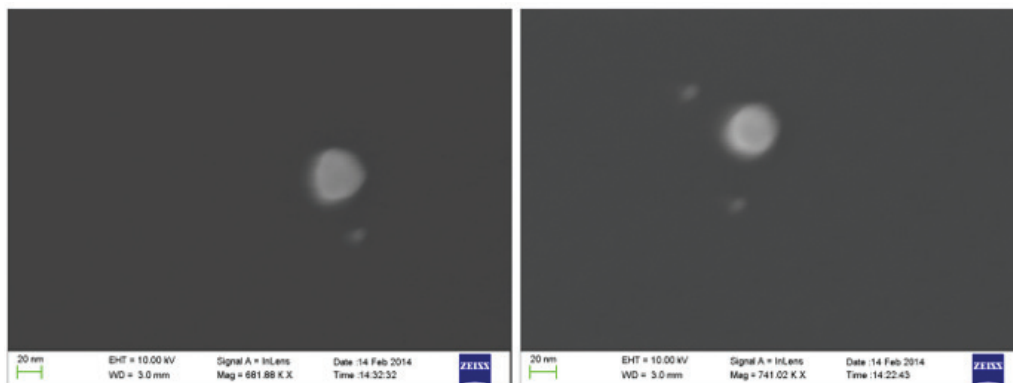


Fig. 3.18: Representative SEM micrographs of biotin functionalized $\varnothing = 50$ nm gold nanoparticles cross linked to similarly functionalized $\varnothing = 10$ nm gold nanoparticles using streptavidin visualizing the number of biotins per nanoparticle.

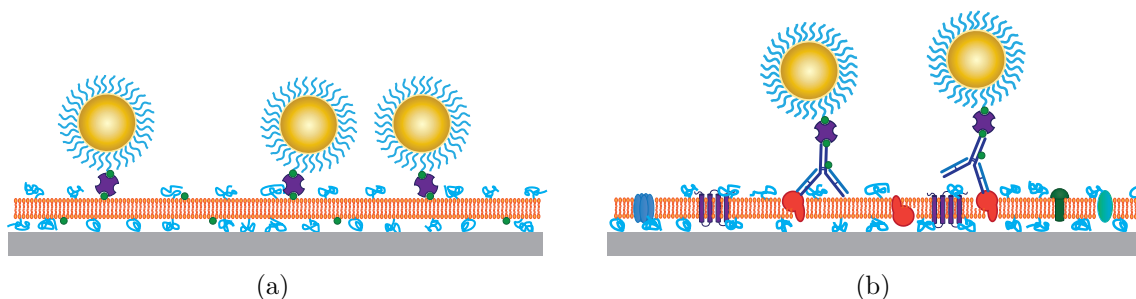


Fig. 3.19: Schematic illustrations of gold nanoparticles bound (a) directly to biotinylated lipids in the membrane and (b) selectively bound to a membrane protein via a biotinylated antibody.

alized nanoparticles were mixed with smaller, similarly prepared nanoparticles, and the resulting mixture was analyzed using scanning electron microscopy (SEM), see Fig. 3.18 for example images of one (left) and two (right) biotins per nanoparticle. This analysis showed little to no aggregation of nanoparticles and one or two biotins per nanoparticle.

In paper IV, aiming at determining the size of nanoparticles, these particles were used as is, binding to biotinylated lipids in the supported membrane, see Fig. 3.19(a). In paper III, however, the aim was to move a single pre-selected membrane component, see Fig. 3.19(b). To make the presented method as versatile as possible, antibodies were used to selectively bind to the pre-selected membrane component. To conjugate the antibody to the gold nanoparticle, the antibody was biotinylated using NHS-biotin, reacting with primary amines on the antibody. The biotinylated antibody was then bound to the SA on the gold nanoparticle, forming an antibody conjugated gold nanoparticle, see Fig. 3.17 right.

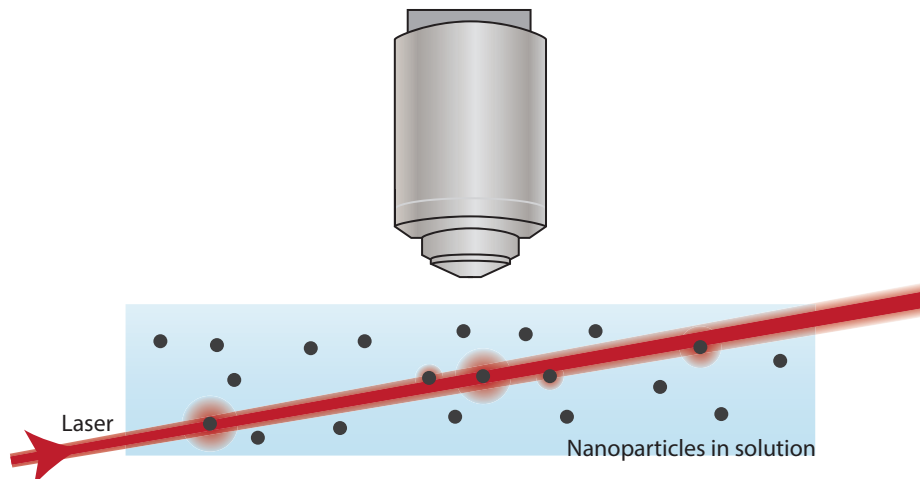


Fig. 3.20: Schematic illustration of the working principle behind NTA. A laser beam is directed through a solution containing nanoparticles, scattering on the nanoparticles. Some of the scattered light is collected by an objective and captured by a camera.

3.4 Size determination of nanometer sized objects

3.4.1 Nanoparticle tracking and analysis

One of the most used methods for measuring the size of nanometer sized objects currently available on the market is nanoparticle tracking and analysis (NTA). The method relies on a laser beam passing through a liquid sample, where the laser light scatters on particles present in the solution, see Fig. 3.20. In contrast to the incident beam, the scattered light is omni-directional and a part of it can be collected by an objective placed above the sample. This scattered light is then captured by a camera at a relatively high frame rate. In the resulting movie, the particles present in the solution will show up as bright dots and using single particle tracking, as discussed in the previous section, the diffusivity of the individual particles can be extracted. The size of the particles can then be extracted by use of the Stokes-Einstein relation, as presented in chapter 2;

$$D = \frac{k_B T}{6\pi\eta r} \quad \Rightarrow \quad r = \frac{k_B T}{6\pi\eta D}, \quad (3.11)$$

From the Stokes-Einstein relation, one can directly deduce that a smaller particle will have a larger diffusivity and that the diffusivity increases with increasing temperature and decreasing viscosity. To get a good measure of the diffusivity (and thus radius) it is therefore important to control these two parameters.

The size of the particle can, in principle, also be extracted from the scattering intensity, given that all particles in the sample are of equal optical density. A larger particle will have a larger scattering cross section and will therefore appear brighter. While this works in theory, there is an intrinsic issue with the geometry of the instrument. To make the instrument as easy to use as possible it is designed for measuring particles free in suspension and the particles will therefore diffuse in three dimensions, while the imaging is inherently two-dimensional. Together with the Gaussian profile

of the laser beam and the fact that the laser beam is deeper than the focal plane due to sub-perfect collimation of the beam, lead up to large errors in size determination based on scattering alone and a very bad correlation between the size determined by scattering and by diffusivity. The root cause of the problem is that out of focus particles, particularly large ones, scatter sufficiently to be captured by the camera but not as much as they would have done if they were in the focal plane. Further, since smaller sized out-of-focus particles risk not being detected at all due to their lower scattering intensity, there is a risk of the produced particle size histograms being biased towards larger particles.

Additionally, the combination of three-dimensional diffusion and two-dimensional imaging, leads to a bias towards shorter track lengths, since the particles freely can diffuse out of the imaging plane. The average track length $\langle N \rangle$ can be estimated by:

$$\langle N \rangle = \frac{\Delta t}{\Delta t_0} = \frac{z_R^2}{2D\Delta t_0}, \quad (3.12)$$

where Δt is the time the particle resides in the focal plane, Δt_0 is the time between two consecutive frame rates and z_R is the Rayleigh length (the length scale of the focal depth). For NTA, $z_R = 5 \mu\text{m}$ and $\Delta t_0 = 1/30\text{s}$, of $\varnothing = 100 \text{nm}$ nanoparticles, $D = 4.4 \mu\text{m}^2/\text{s}$, the estimated average track length is 85 frames.^[107]

Considering that the standard error of the mean follows $SE_{\bar{x}} = s/\sqrt{n}$, where n is the number of observations, in this case the length of a track, a longer track will yield a better estimate of the true size of a particle. Hence, NTA, being biased towards short tracks, yields poor precision when measuring the size of a specific object, with a relative error in the size determination of 9%. However, this shortcoming can be somewhat reduced by longer recordings, increasing the amount of statistics, since this yields an accurate determination of the size profile of the ensemble average.

3.4.2 Scanning electron microscopy

Another method for measuring the size of nanoparticles, which has been used as a control measure in the work presented in this thesis is SEM. As can be gathered from the name, electrons are used in SEM. The advantage of using electrons for imaging as compared to photons as used in optical microscopy, discussed in detail earlier in this chapter, is that the wavelength of the electrons is significantly shorter than that of visible light photons. Shorter wavelength yields higher resolution, which in turn enables larger magnification.

Like a camera is used to capture photons in an optical microscope, electron detectors are used to capture electrons in an SEM. Many different such detectors exist and they detect different types of electrons with respect to *e.g.* energy, but this has not been the focus of this thesis work and will thus not be discussed in depth.

With the higher resolution and magnification provided by an SEM, single gold nanoparticles can be depicted, see Fig. 3.21(a) (this is in contrast to SEEC or EWS where the point spread function makes the gold nanoparticles appear significantly larger than they are). From a micrograph, like the one presented in Fig. 3.21(a), the size of individual nanoparticles can be evaluated directly by measuring the depicted

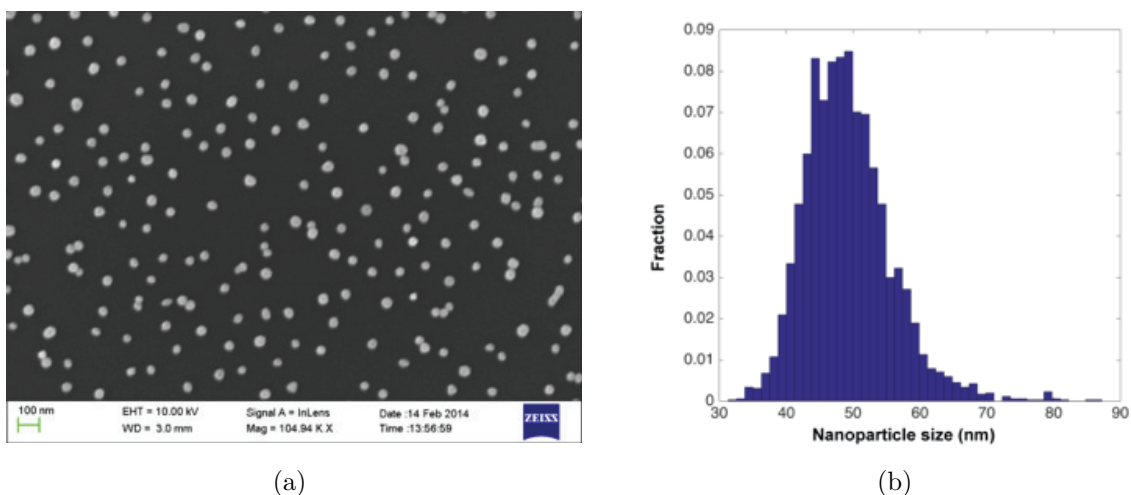


Fig. 3.21: (a) SEM micrograph of $\varnothing = 50$ nm gold nanoparticles with a size distribution shown in (b).

area of the nanoparticle, and the size distribution of the nanoparticles in the sample can be summarized in a histogram, see Fig. 3.21(b).

3.4.3 Two-dimensional flow nanometry

In paper IV is presented a new technique for measuring the size of nanoparticles, combining some of the ease of use of NTA with some of the measurement precision of SEM-based size determination. This is achieved by limiting the diffusion of the nanoparticles to two dimension, thus forcing them to stay longer in the focal plane, as compared to NTA, yielding longer tracks and therefore better accuracy. While this sounds good in theory, the reality is that in doing so, one does not measure the diffusivity of the object of interest anymore but rather that of the linkers. Using an SLB, the diffusivity of the linker in the SLB is significantly slower than that of a nanoparticle in solution. This will turn out advantageous in a later step, but it means that simply measuring the diffusivity of the linked particles tells nothing about their size.

Drawing from theory presented earlier in this chapter, it is evident that the force acting upon a particle bound to an SLB from an applied bulk flow will scale with the size of the nanoparticle and a larger force acting upon the particle means that it should move faster along the flow direction. This can also be experimentally verified, see Fig. 3.22.

However, while this is true, the movement will also be influenced by the linking of the particle to the membrane, or more specifically the membrane friction experienced by the linkers. In the case of multi-valency the number of linkers affect the membrane friction of the linker collective. Increasing the number of linkers linking a nanoparticle to the SLB increases the membrane friction experienced by the nanoparticle. In turn, this leads to a decreased particle velocity at a constant applied force.

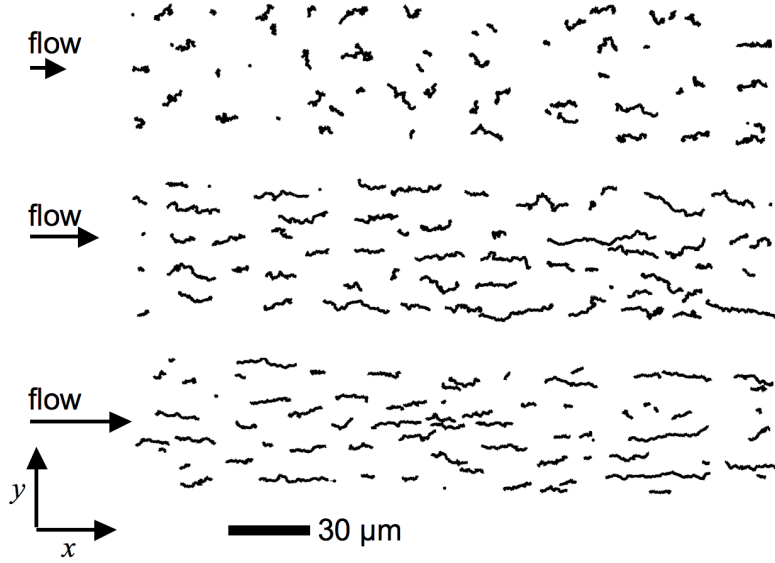


Fig. 3.22: Representative SPT tracks of $\varnothing = 50$ nm gold nanoparticles with an applied flow of 5 (top), 10 (middle) and $15 \mu\text{L}/\text{min}$ (bottom) applied from left to right in the figure.

Thus, the movement of a tethered nanoparticle under an applied shear flow is the sum of two effects; i) a deterministic movement that is due to the shear force from the bulk flow and ii) a stochastic diffusion that is due to collisions with water molecules. Fortunately, the Einstein-Smoluchowski relation connects the directed and random movement as it relates the object's mobility μ , defined by:

$$\mu = \frac{v_x}{F_{\text{shear}}}, \quad (3.13)$$

with the diffusion coefficient of the linker, D_{link} , via

$$\mu = \frac{D_{\text{link}}}{k_B T}. \quad (3.14)$$

This relation can be derived from the fluctuation-dissipation theorem. The fluctuation-dissipation theorem states that the forces that cause random fluctuations in the system at equilibrium, also create dissipation (or friction) when the system is subject to a non-random force. The non-random force in this case is the shear force that creates directed movement of the nanoparticle while the random force is the random lipid collisions experienced by the linker in the membrane. Combining eqs. 3.13 and 3.14 yields:

$$F_{\text{shear}} = \frac{k_B T v_x}{D_{\text{link}}}. \quad (3.15)$$

Since v_x and D_{link} can be extracted independently from the particle trajectories, see Fig. 3.23, this means that the hydrodynamic shear force can be calculated directly from the SPT tracks. As both v_x and D_{link} depend on the mobility of the linkers, any linker property drops out when combining Eqs. 3.13 and 3.14 into Eq. 3.15. Hence,

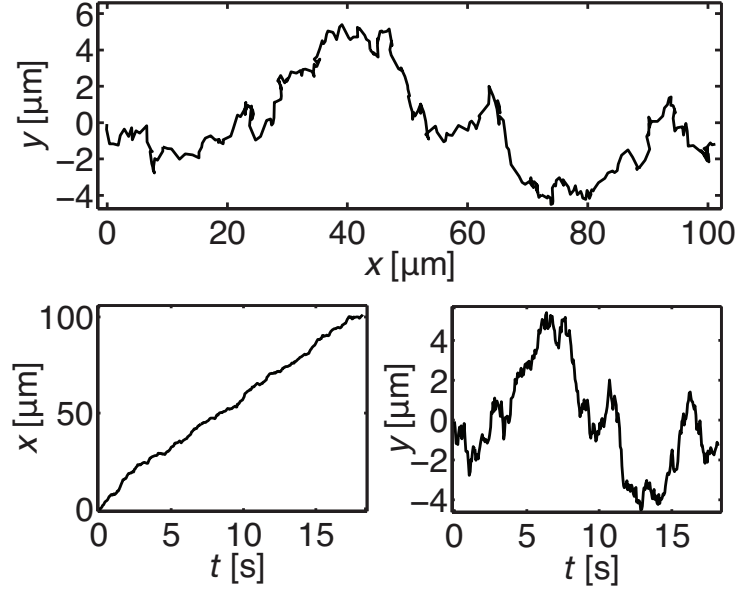


Fig. 3.23: An SPT-track, see top, of a particle subject to a shear flow from left to right. With the shear flow only along the x -axis, the influence of the shear flow is not seen along the y -axis when the movement is split up into x -, and y -components, see bottom.

the hydrodynamic shear force acting on a nanoparticle can be determined directly from v_x and D_{link} using Eq. 3.15.[†]

The hydrodynamic shear force acting on a nanoparticle, with hydrodynamic radius r , tethered to an SLB, subject to a flow velocity v_0 , under laminar flow conditions is:

$$F_{\text{shear}}(r) = A\eta v_0 r(r + \lambda), \quad (3.16)$$

where A is a factor that accounts for the inhomogeneous flow profile around the nanoparticle and λ is the slip length. The slip length is a correction factor that accounts for the non-validity of the no-slip condition under these conditions. The no-slip condition states that the flow velocity along a fluid-solid interface must be zero since the solid cannot move, when the surface is covered by a high-viscosity fluid like the SLB, however, this condition does not hold and the flow velocity along the boundary will be non-zero. The slip length gives the apparent distance into the solid where the fluid is zero. Both A and λ are difficult to predict theoretically, but can be determined by calibration using, in this case, a well defined nanoparticle distribution.

Thus, measuring v_x and D_{link} by SPT it is possible to measure the hydrodynamic size of nanometer sized objects, under the condition that a suitable linker is found and they are visible under the microscope. In paper IV this method was used to measure the size of lipid vesicles and gold nanoparticles, as summarized in chapter 4.4.

[†]Note that these equations only hold as long as the diffusion coefficient of the linked object is dominated by the diffusion coefficient of the linker itself. This is fulfilled for typical linkers (diffusion coefficient below $1 \mu\text{m}^2/\text{s}$) given that the hydrodynamic radius, r , of the freely diffusing object is below around 200 nm.

Chapter 4:

Summary of results and reflections

In this chapter short summaries of the results obtained in the four papers appended to this thesis are provided. The chapter is divided into one section covering each paper. For a deeper discussion on the results, the reader is referred to the respective paper.

4.1 Paper I

Paper I deals with the influence of a 10 nm high gold barrier situated on the floor of a microfluidic channel on the efficiency by which membrane associated molecules, lipids and the membrane binding cholera toxin B subunit (CTB), can be accumulated and separated.^[103] The reason for introducing the gold barrier was two-fold. Firstly, it confines the SLB to the center of the channel where the bulk flow is relatively constant. Secondly, it had previously been observed that the SLB has a tendency of creeping onto the walls of the channel, with the implication that accumulated material at the front of the SLB could escape, thus decreasing the efficiency of the accumulation.^[91] In addition to the gold barrier, the channel was made wider than in the previous studies, to further flatten the bulk flow profile above the SLB.

To quantify the improvements of the gold barrier concept, accumulation experiments with the head-group labeled phospholipid Lissamine rhodamine B 1,2-dihexadecanoyl-sn-glycero-3-phosphoethanolamine (R-DHPE) were carried out. The fluorescent dye molecule increases the size of the head-group of R-DHPE with the head protruding from a POPC SLB. The protrusion is less than a nanometer, which is still enough for the labeled lipids to move $\sim 5\%$ faster than the surrounding, non-labeled, lipids while not substantially influence the drift velocity of the membrane.^[108] Furthermore, the molecular protrusion is too large to fit in the hydrated film between the SLB and the support, which means that the SLB front acts as a molecular sieve with the labeled lipids accumulating at the SLB front.

In Figs. 4.1(a) to (c) is shown a time lapse of an SLB being shear-driven into the barrier-containing right arm of a microfluidic channel. Furthermore, in Figs. 4.1(c) and (d) is a comparison between the accumulation profiles with and without barrier, where the solid lines indicate constant intensity. As can be seen, the barrier dramatically flattens the hyperbolic profile of the bare channel so that the resulting accumulation profile is essentially perpendicular to the bulk flow.

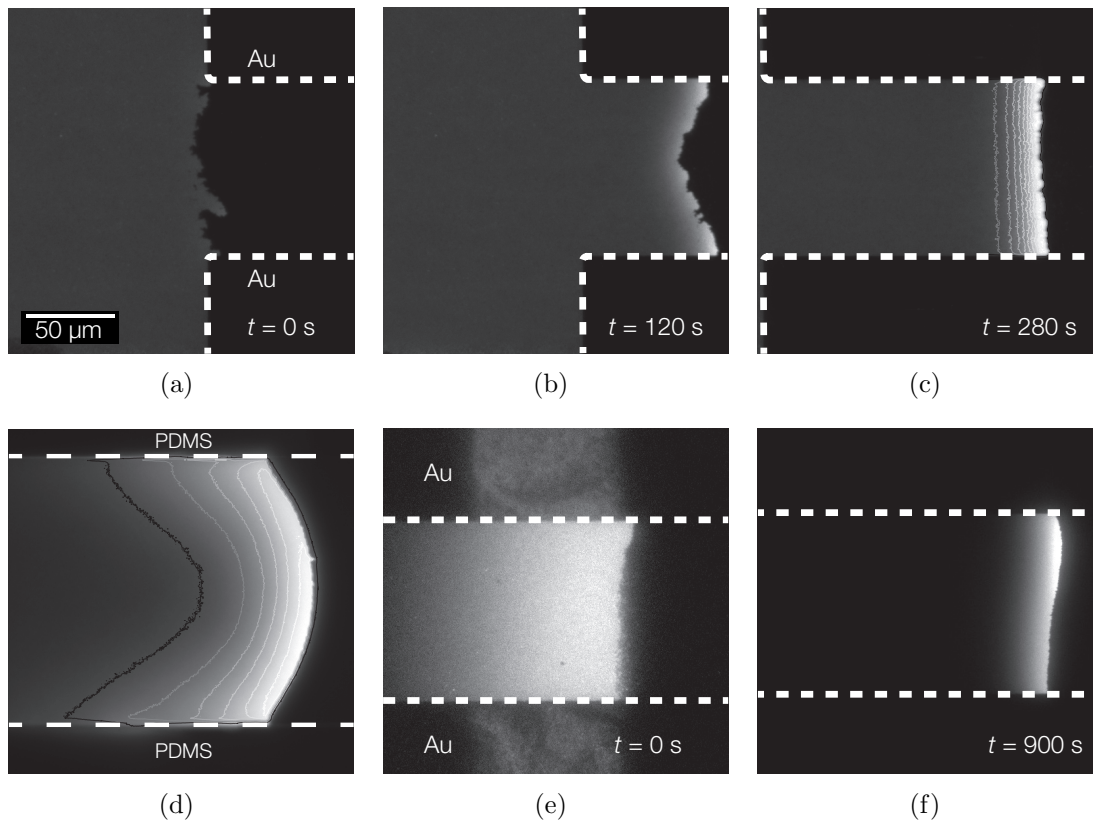


Fig. 4.1: Fluorescence micrographs of shear-driven SLBs. (a) to (c) shows a time-lapse recording of an SLB confined to the center of the microfluidic channel as it is driven forward. (d) shows the accumulation shape without gold barriers. The contour lines in (c) and (d) indicate constant intensity. (e) and (f) shows a shear-driven SLB with a fluorescently labeled plug.

Using a channel also enables the use of a so called plug, see Figs. 4.1(e) and (f). The plug is a small patch of material different to the main SLB that is formed in front of the SLB so that all of the fluorescent material is visible in the field of view of the camera at all times. Note in particular the difference in the time evolution of the intensity profile for an entirely labeled SLB, Fig. 4.2(a), and the plug, Fig. 4.2(b), where the intensity at the back of the SLB approaches zero. The advantage of this approach is that the amount of labeled material in the experiment is low and since all of the labeled species are always in the frame of the camera, it simplifies certain analyses since the SLB behind the front does not contain any fluorescence. When accumulating and separating CTB, such a plug of G_{M1} containing SLB was formed in front of a pure POPC SLB. CTB was then injected and bound exclusively to the G_{M1} plug. CTB is one of the parts of the cholera toxin and is responsible for the toxin binding to an SLB, whereas subunits A1 and A2 are the pore forming constituents of the toxin.^[109;110] Five of the B subunits constitute CTB and each of the subunits can bind to one G_{M1} in the SLB.^[111] Since not every CTB will be bound to a G_{M1} at all times, the multivalency of CTB could be studied by hydrodynamic forces since

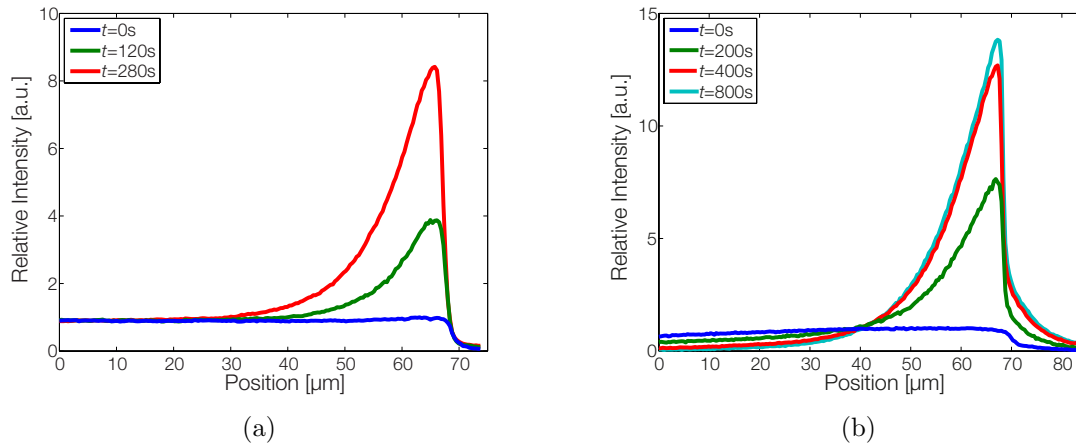


Fig. 4.2: The time evolution of the intensity profile for (a) an entirely labeled SLB as seen in Fig. 4.1(a) to (c), and (b) an unlabeled SLB with a labeled plug, as seen in Fig. 4.1(e) to (f).

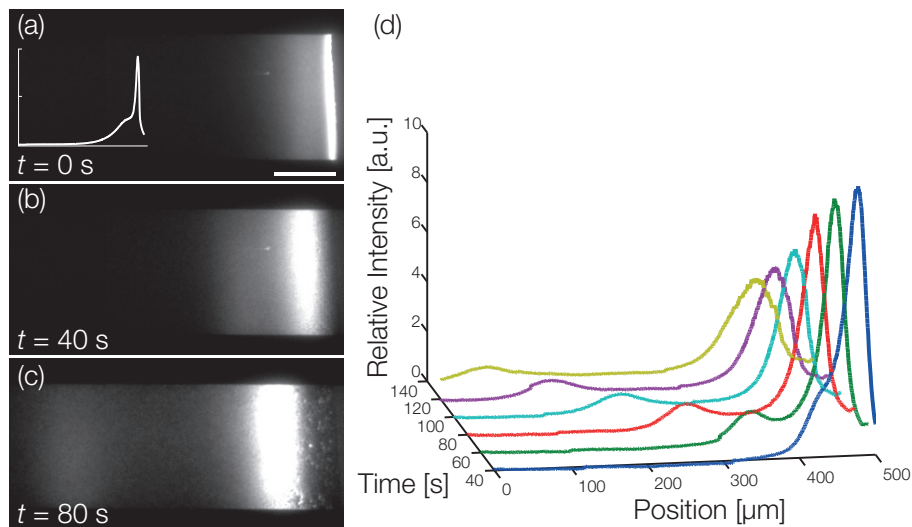


Fig. 4.3: (a) to (c) shows a time-lapse of the separation of CTB into two populations based on the number of bilayer anchors. (d) shows the time evolution of the intensity profiles. Note that the intensity between the populations drops to zero, indicating total separation. The inset in (a) shows the intensity profile at $t=0$ s, not shown in (d). The scale bar is $50\ \mu\text{m}$.

every G_{M1} anchor point in the SLB increases the membrane friction. Therefore, the larger the number of anchoring points, the slower the CTB would move. So, after accumulation of CTB at the front of an SLB, the flow was reversed and the CTB was separated into two clearly visible bands moving through the SLB at different speeds, see Fig. 4.3.

Moreover, thanks to the fact that the back of the SLB does not contain any CTB, total separation, *i.e* a black (empty) band, between the different populations could be achieved, see the curve corresponding to $t = 140$ s in Fig. 4.3(d). The total separation between the two populations is critical if *e.g.* the kinetics of the different populations are of interest or allow elution and further analysis of the separated components.

4.2 Paper II

Paper II presents a label-free diffusion study using SEEC substrates as discussed in chapter 3.^[112] Two systems with peripheral membrane proteins were studied, 1) streptavidin (SA) bound to a biotinylated lipid (biotin-PE; 1,2-dipalmitoyl-sn-glycero-3-phospho-ethanolamine-N-(cap biotinyl)) in the SLB and 2) the soluble part of the adhesion protein rat CD2 (CD2) found on the surface of T cells^[113;114] bound to a nickel chelating lipid (DGS-NTA) in the SLB via a His-tag. In order to validate our data, we also performed control experiments using labeled proteins to 1) compare the diffusion with and without labels, 2) compare with data from fluorescence experiments, 3) compare the measured diffusivities with those obtained using FRAP.

Figures 4.4(a) and (b) show micrograph time-lapse recordings of the release of accumulated fluorescently labeled streptavidin (SA-488). SA-488 was accumulated under the tip of a micropipette using a negative pressure applied to the micropipette. At $t = 0$ s the pressure was released and the accumulated proteins diffuse out of the trap. In Figs. 4.4(c) and (d) the intensity of the center of the accumulated spot versus time is shown together with a fit to Eq. (3.10). Also shown is the radial intensity of the accumulated spot, where in Fig. 4.4(c) it can be seen that at $t = 0$ s the surface coverage of SA-488 is 40 times the equilibrium coverage at this biotin-concentration in the SLB corresponding to $1.8 \cdot 10^4$ proteins/ μm^2 or a surface coverage of 45%.

We found that the measured diffusivity in the SEEC setup was slightly higher than that measured using FRAP, see Fig. 4.5. We suggest that this is due to the high surface coverage underneath the pipette tip creating electrostatic repulsion between the accumulated species that would force the proteins apart faster than would be the case in a diffusion dominated system. To validate this hypothesis, the diffusivity using data obtained from directly after the hydrodynamic trap was turned off were compared with the diffusivity obtained from the same data but with the first 10 s truncated. This showed that the diffusivity decreased with time in the hydrodynamic trap and would suggest that there indeed is some repulsion between the accumulated species at high coverage.

Moreover, when using the SEEC substrate we have a unique ability to compare the diffusivity of the unlabeled proteins with that of labeled proteins under more or less the exact same circumstances. For both of the studied proteins, the result of the

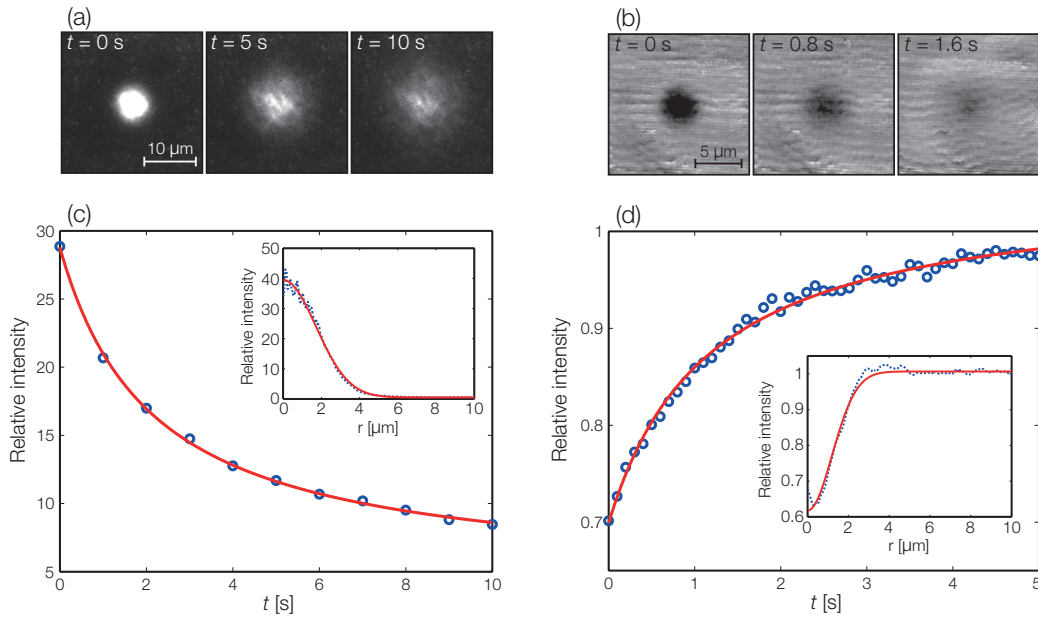


Fig. 4.4: Accumulation of fluorescently labeled streptavidin using hydrodynamic forces using (a) fluorescence and (b) SEEC imaging. The trap is turned off at $t = 0$ s and the accumulated proteins diffuse out of the trap. The intensity measured in the center of the accumulated spot with respect to time is shown in (c) and (d) with the insets showing the radial intensity profile at $t = 0$ s. The solid lines represent a fit to Eq. (3.10).

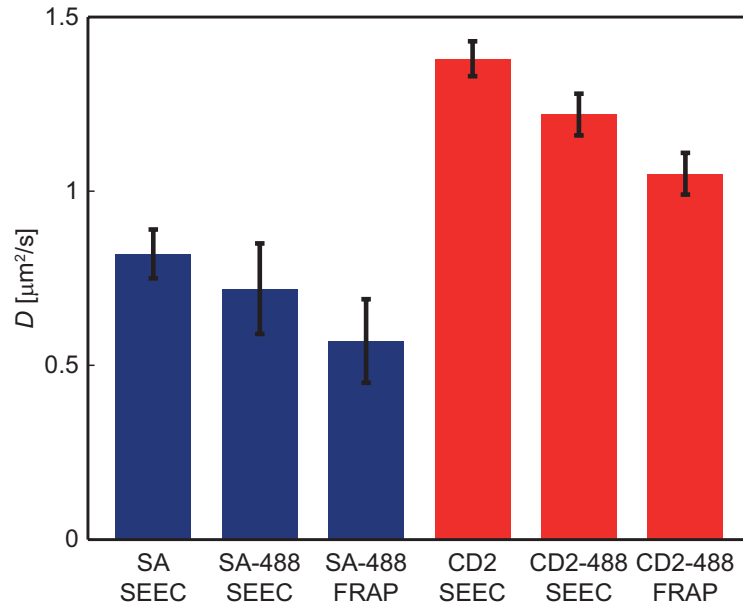


Fig. 4.5: The diffusivities for streptavidin (blue) and CD2 (red) measured using SEEC imaging. The diffusivities were measured using both labeled and non-labeled proteins. For comparison, the diffusivities measured using FRAP is also included. The error bars correspond to ± 1 standard deviation from at least three measurements.

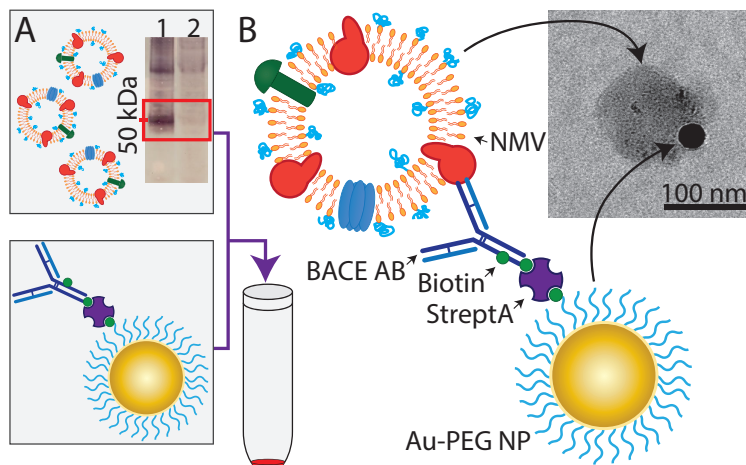


Fig. 4.6: (A) BACE1 containing native membrane vesicles, Western blot in inset clearly indicating BACE1 expression in lane 1 in comparison to mock membrane in lane 2, were pre-incubated (B) with monoclonal antibody-modified gold nanoparticles, forming a native membrane vesicle-gold nanoparticle construct, as visualized by the TEM micrograph inset. The arrows indicate the location of the native membrane vesicle and the gold nanoparticle, respectively.

fluorescent label is a decrease of the diffusivity of $\sim 12\%$, that most probably is due to interaction between the labels and the SLB as discussed by Saxton and Jacobson^[115] and Yoshina *et al.*^[116]

Label-free measurements of the diffusivity of membrane-associated molecules is not only interesting since it highlights the influence of the fluorophore but also, potentially more importantly, a method by which the diffusivity of molecules that are difficult to label or where the fluorophore is expected to have a large influence on the diffusivity can be measured.

4.3 Paper III

Paper III presents a technique where gold nanoparticles are conjugated to the ectodomain of a membrane protein,^[117] see Fig. 4.6. As explained in chapter 3, the hydrodynamic force acting upon a membrane species is proportional with the cross-sectional area exposed to the flow. Thus, artificially increasing this area by conjugation of a comparatively large gold nanoparticle* also increases the force acting upon the selected species from an applied bulk flow.

If the gold nanoparticle is large enough, the bulk flow required to move the particle and the membrane protein to which it is conjugated can be small enough so that it influences only the movement of the gold nanoparticle and selected species while not significantly affecting the movement of the other membrane species.

*The ectodomain size of the membrane protein used in the study is a few nm^2 , whereas the gold nanoparticle has a cross-sectional area of $\sim 10^4 \text{nm}^2$, so conjugation of the latter to the former enlarges the ectodomain of the membrane protein by close to a factor 10^4

The idea was demonstrated by in-membrane purification of the integral membrane protein β -secretase 1 (BACE1) from cell-derived native membrane vesicles (NMV). This transmembrane protease contributes to the cleavage of the amyloid precursor protein into amyloid- β peptides, a process implicated in the pathogenesis of Alzheimer's disease.^[118] Here BACE1 was selected because of its structure comprising a single transmembrane domain and a large ectodomain that can be efficiently targeted by a monoclonal antibody. As mobile phase for the extraction, a native-derived supported lipid bilayer was formed by spontaneous vesicle rupture on the glass floor of a microfluidic channel. This lipid membrane was formed from the BACE1-containing NMVs diluted with small unilamellar vesicles (SUVs) made from synthetic lipids, which aid the rupture and bilayer formation from membrane vesicles.^[55;56] To prevent BACE1 and other membrane proteins contained in the NMVs from adsorbing to the glass surface and thereby lose their mobility, prior to the membrane formation, lipids with poly(ethylene)glycol (PEG) modified head groups were also introduced in the NMVs by sonication-induced lipid transfer from SUVs containing such lipids.^[57]

In the experiments, approximately 40% of the gold nanoparticles visible on the surface became mobile upon rupture of vesicles into a supported membrane, with the non-mobile fraction corresponding to BACE1 ectodomains facing the substrate, BACE1 located in non-ruptured vesicles, unspecifically adsorbed to the substrate or defects in the membrane or gold nanoparticles non-specifically bound to the membrane or membrane defects. Two distinct populations were visible among the mobile 40%, see Fig. 4.7(a), as evidenced by their different diffusivities, $0.73 \pm 0.09 \mu\text{m}^2/\text{s}$ and $1.51 \pm 0.25 \mu\text{m}^2/\text{s}$ (mean \pm one standard deviation from $n = 6$ measurements), respectively. The faster of these two populations have a diffusivity on the same order as is commonly observed for lipids in a supported membrane, whereas the slower fraction, indicated in red, is closer to the diffusivity expected for a transmembrane protein with a transmembrane part with a diameter of BACE1 according to the Saffman-Delbrück model.[†]^[119]

In control experiments, where a mock membrane sample prepared in the same way as the BACE1 expressing sample but not transfected with the gene for BACE1 expression, only the faster of the two populations are present whereas the slower population is completely absent, see Fig. 4.7(b).

The microfluidic setup used for the experiments enabled us to apply a weak hydrodynamic bulk flow above the supported membrane, similar to what was done to

[†]The Saffman-Delbrück model states that the diffusivity of a cylindrical membrane inclusion, with radius r , in a membrane with thickness, h , a dynamic viscosity of η_m and a dynamic viscosity of the surrounding fluid of η_f is:

$$D_{\text{SD}} = \frac{k_{\text{B}}T}{4\pi\eta_m h} \left(\log \frac{\eta_m h}{\eta_f r} - \gamma \right),$$

where $\gamma = 0.5772$ is Euler's constant. For a single α -helix membrane protein like BACE1 with an intrusion radius of $r = 0.7 \text{ nm}$, in a non-supported membrane with a thickness of $h = 5 \text{ nm}$ and a viscosity of $\eta_m \approx 0.1 \text{ Pa}\cdot\text{s}$, surrounded by water with a viscosity of $\eta_f = 10^{-3} \text{ Pa}\cdot\text{s}$, the Saffman-Delbrück model yields a diffusivity of $D_{\text{SD}} \approx 3.9 \mu\text{m}^2/\text{s}$, similar to the diffusivity of lipids in a non-supported membrane, in agreement with the diffusivity values of BACE1 in supported membranes being of the same order of magnitude as the diffusivity of lipids in the membrane.

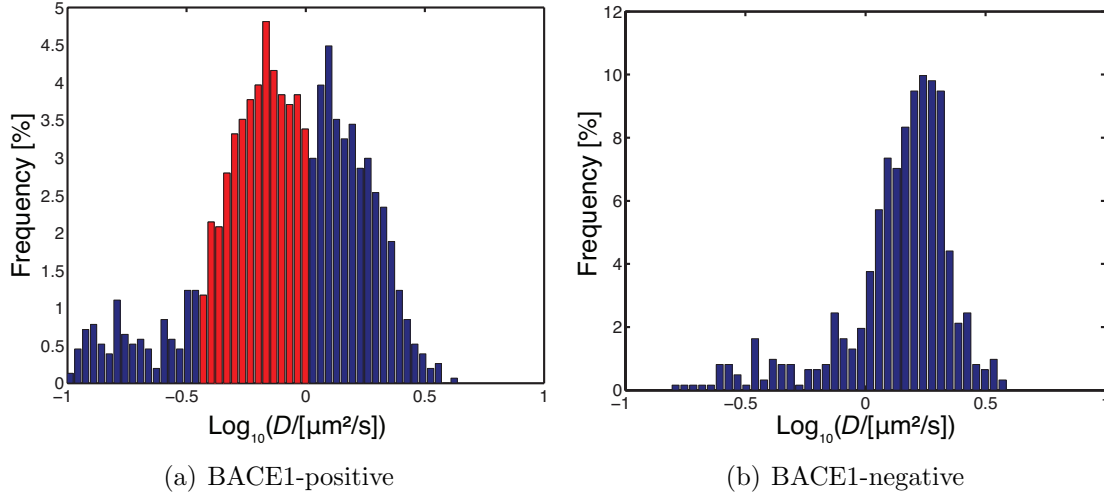


Fig. 4.7: Diffusion histograms resulting from analysis of single particle tracking of gold nanoparticles in (a) BACE1-positive membrane and (b) mock membrane negative control. In (a) the slower population, completely absent in (b), is highlighted in red.

achieve protein accumulation in paper I, but taking advantage of the large cross-sectional area of the gold nanoparticle, BACE1 could be accumulated at a bulk flow two orders of magnitude smaller than those used in paper I.

The accumulation was carried out against a membrane barrier, created by injecting the membrane material into a four-arm microfluidic channel, similar to the one used in paper I, with a counter flow. This results in a semi-continuous supported membrane, spanning one half of the microfluidic device and the membrane edge, presents a barrier, impenetrable for membrane material, similar to the membrane front in paper I. Applying a bulk flow towards the membrane edge will then accumulate the gold nanoparticles in the sample against the membrane edge.

Despite using a significantly lower flow pressure than in paper I, an accumulation factor[‡] of $R = 4 \cdot 10^3$ was achieved; two orders of magnitude larger than what was achieved in paper I, without hydrodynamic kites. This corresponds to an accumulation efficiency, that is the ratio between the accumulation factor and the flow pressure, R/p , that is four orders of magnitude larger. On the other hand, the resulting surface coverage is significantly lower than that achieved in both papers I and II, explained by the significantly lower amount of material in the system as evidenced by the low initial surface coverage. As a matter of fact, roughly 50% of all the gold nanoparticles initially injected in the system are accumulated at the membrane edge.

In addition to purification of BACE1 in a native derived supported membrane, the hydrodynamic kites were used to move BACE1 from one membrane environment to another. Since the function of many membrane proteins is dependent on the membrane environment, this could potentially provide a useful tool for investigating the influence presence of certain membrane components have on the activity of mem-

[‡]The accumulation factor is defined as the ratio of the surface coverages before (Γ) and after (Γ') accumulation, $R = \Gamma'/\Gamma$.

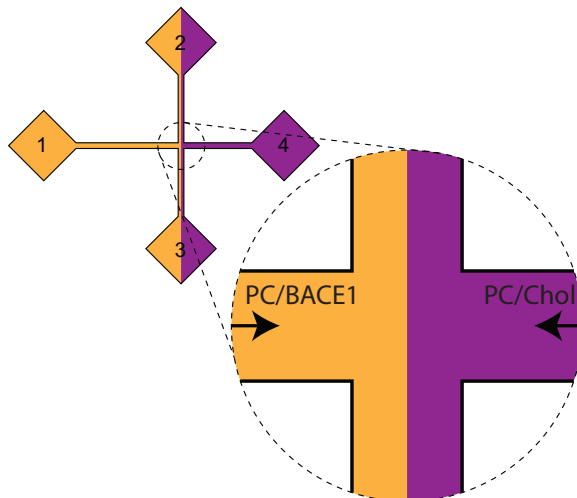


Fig. 4.8: Schematic illustration of how the membrane environment changing setup was created in the microfluidic device. A purely synthetic PC-vesicles containing reconstituted biotinylated BACE1, to which gold nanoparticles were linked via streptavidin, was injected into connection 1, while a PC-vesicles containing 20% cholesterol was injected through connection 4. Connections 2 and 3 were configured as outlets.

brane proteins. As a first step towards more involving studies, we investigated the influence cholesterol has on the diffusivity of BACE1 in the membrane and whether it was affected similarly to the rest of the membrane. For this, biotinylated BACE1 reconstituted into purely synthetic PC-lipid vesicles were used and gold nanoparticles functionalized with streptavidin were bound to the proteins. The gold nanoparticles were used to move BACE1 from the pure PC membrane to a membrane containing 20% cholesterol, see Fig. 4.8 for a schematic illustration of the setup. As can be seen from the diffusivity histograms in Fig. 4.9, there are two populations with distinctively different diffusivities, just as was the case with the BACE1 in NMVs. The diffusivities of the two populations in the pure PC-membrane more or less coincide with the diffusivities measured on the native derived supported membrane system. Upon entering the cholesterol-rich membrane there was a significant decrease in the diffusivities of both populations, with the slower population decreasing from $D_{\text{PC}} = 0.89 \pm 0.22 \mu\text{m}^2/\text{s}$ to $D_{\text{PC/Chol}} = 0.53 \pm 0.11 \mu\text{m}^2/\text{s}$ and the non-specifically bound population decreasing by a similar percentage.

The fact that the faster, non-specific, population showed up in all experiments, regardless of whether there were any biological membrane material in the membrane or it was purely synthetic and regardless of whether BACE1 was present or not, indicates that the non-specific interaction between the gold nanoparticles and the membrane was most probably due to PEG on the gold nanoparticles and in the membrane interacting.

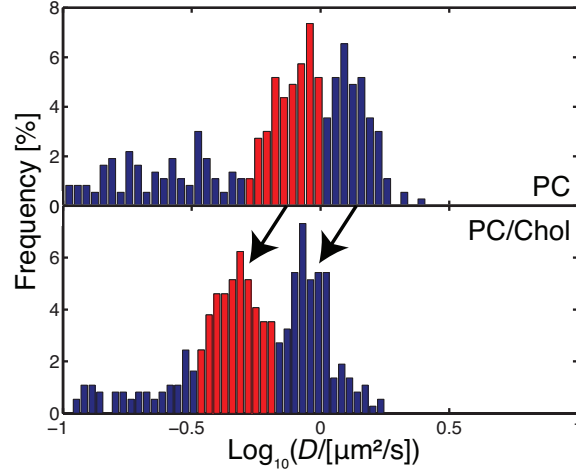


Fig. 4.9: Diffusion histograms illustrating the decrease in diffusivity when moving BACE1 from a membrane containing no cholesterol to one containing 20% cholesterol. The slower of the two populations are highlighted in red.

4.4 Paper IV

Paper IV presents an extension of the work presented in paper III and submitted work by S. Block *et al.*,^[120] investigating size determination of nanoparticles linked to a supported membrane.^[121] For this, a microfluidic setup similar to the one used in paper III was used, with a four arm microfluidic device, though for the purposes of the study, a straight channel with two connections could have been used. As described in chapter 3.4.3, the size determination is based on SPT of nanoparticles tethered to an SLB. Under stagnant condition, these nanoparticles will diffuse on the SLB, but the diffusivity is determined by linker and SLB properties rather than by the size of the nanoparticle,^[116] unlike the situation in NTA. Applying a hydrodynamic flow through the microfluidic channel will cause the nanoparticles to move along the direction of the flow, and this deterministic movement will be superimposed with the stochastic diffusion observed under stagnant conditions. Deconvolution the movement into these two contributions, see Fig. 3.23, gives the velocity of the nanoparticle, v_x and its diffusivity, determined by the linkers, D_{link} . From these the hydrodynamic force acting on the nanoparticle can be calculated and the hydrodynamic radius of the nanoparticle can be extracted.

This method was verified on different samples, gold nanoparticles and lipid vesicles. But before the measurements could be done, the missing factors in Eq. 3.16, A and λ needed to be determined by calibration of the setup. These calibration experiments were carried out on gold nanoparticle solutions with relatively narrow size distributions, using the distribution as acquired using SEM as a reference, see Fig. 4.10(a) and (c). In the end it proved that the slip length had only a small impact on the extracted size for nanoparticles in the studied size range, as evidenced by Fig. 4.10(b) and (d), where the bars correspond to a slip length of 24.4 nm and the dashed line 64.5 nm, given by two types of fitting to the calibration experiments.

Since the SLB is an isotropic medium, the diffusivity is expected to be the same

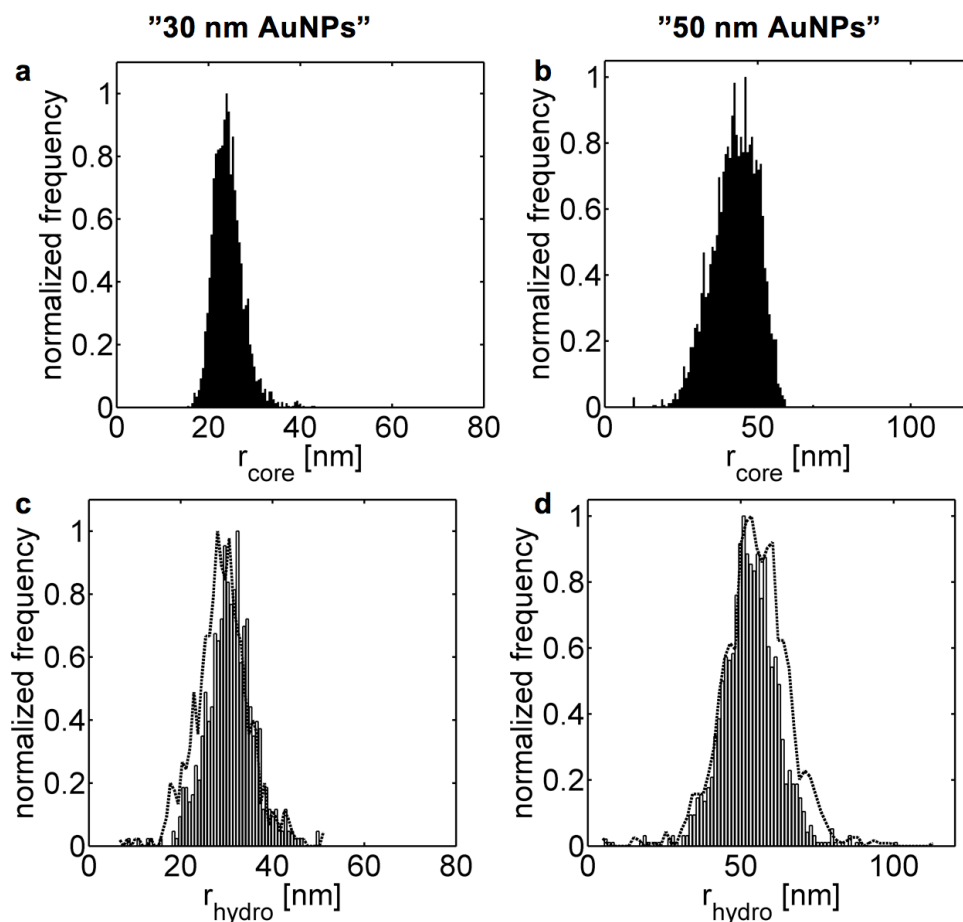


Fig. 4.10: Comparison of size distributions of two different sizes of gold nanoparticles determined using electron microscopy (a, c) and using two-dimensional flow nanometry (b, d). The bars in (b) and (d) indicate the extracted size distributions using a slip length of 24.4 nm, while the dashed lines correspond a slip length of 64.5 nm. The distributions are essentially identical, only shifted by 5 nm, attributed to the 5 nm PEG corona on the surface of the gold nanoparticles which is invisible using SEM.

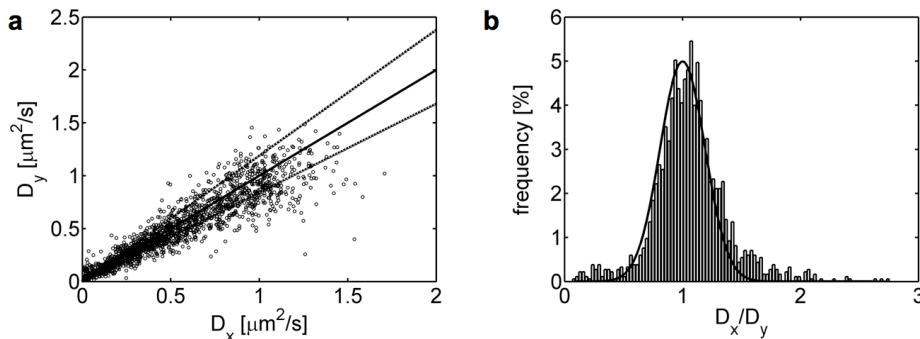


Fig. 4.11: Comparison of the 1D diffusion coefficients D_x and D_y of gold nanoparticles with a hydrodynamic radius of 30 nm, extracted using the decomposition method illustrated in Fig. 3.23. In (a) is a parameter plot of D_x vs. D_y and in (b) is the normalized probability distribution of the ratio D_x / D_y . The solid line in (a) indicates the expected 1:1 relation between D_x and D_y . The dashed lines give the expected error interval.

along regardless of direction, despite the apparent differences between the movement along the x axis (parallel to the flow direction) and the y axis (perpendicular). Fig. 4.11(a) shows that the correlation between one-dimensional diffusivities, D_x and D_y , is high and this demonstrates that the data extraction procedure successfully decouples the directed and the random movement of the nanoparticles.

Comparing size distributions measured using the two-dimensional flow nanometry approach, to size distributions of the same samples measured using SEM, as seen in Fig. 4.10, give the size distributions as very similar between the techniques. Both samples' distributions are shifted to 5 nm larger values in the case of the two-dimensional flow nanometry, something attributed to the ~ 5 nm PEG-corona that the nanoparticles are functionalized with. While the PEG-corona adds to the hydrodynamic radius of the nanoparticle it is virtually invisible in SEM.^[122]

As previously stated, lipid vesicles were also measured using this technique. The vesicles were tethered to the SLB using cholesterol-anchored double-stranded DNA, as discussed in chapter 3.2.2. The resulting size distributions were cross-checked with NTA and dynamic light scattering (DLS), see Fig. 4.12. All three distributions look similar, the only notable difference is that the size distribution from NTA has a rather dramatic cut-off at a radius of approximately 25 nm, that can not be seen in either of the other two setups.

In this paper we proved that by restriction of a nanoparticles movement to a two dimensional viscous fluid interface, it was possible to extract a more accurate size distribution of biological nanoparticles than is possible using commercially available alternatives, yielding, in the case of gold nanoparticles, an accuracy almost as good as what is achieved using electron microscopy.

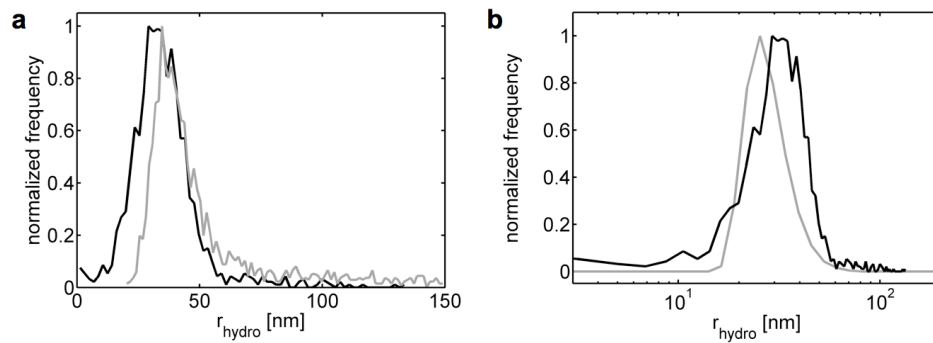


Fig. 4.12: Comparison between size distributions for the same vesicle sample. In both (a) and (b) the size distribution obtained from two-dimensional flow nanometry is shown in black. In (a) this is compared to the size distribution from NTA in gray. In (b) the two-dimensional flow nanometry-derived distribution is compared to DLS (gray).

Chapter 5:

Outlook - deterministic sorting

The main aim of this thesis, when I started my PhD studies almost five years ago was to be able to accumulate and purify and sort membrane proteins in a crude cell membrane. Ideally, there was supposed to be a way to get the purified membrane proteins out of the microfluidic device. Looking at the hydrodynamic kites used to enrich the transmembrane protein BACE1 in paper III, at least part of this aim was actually fulfilled. However, studying the hydrodynamic kites under an applied bulk flow provided some interesting insights that led us to be able to determine the size of the nanoparticles, an accomplishment that might turn out to be of high practical relevance.

Since the nanoparticles are tethered to a lipid bilayer, limiting their movement to two dimensions, following the direction of the flow, the step from nanometry to nano-sorting is quite short. Adding a computer-controlled microfluidic device, with a slightly updated design where one of the arms has been split, transforming the four-arm channel into a five-arm that allows for sorting into two populations, to the size determination as described in paper IV gives us the possibility of sorting nanoparticles depending on their size. Such nano-sorting could potentially allow valuable insight into the decisive factors for the function of biological nanoparticles. One such group of nanoparticles are the so called exosomes.

Briefly; exosomes are a type of extracellular vesicles with endosomal origin, with a protein spectrum reflecting their cell origin, overlaid with a exosome specific signal.^[123] Exosomes have been found to carry RNA as well as proteins.^[124] Exosomes have been found to be able to transfer molecules from one cell to another,^[124] which is believed to be part of the adaptive immune response to pathogens affecting the protein production in the recipient cell.^[125] Hence, exosomes are potentially very important extracellular vesicles, but there is a difficulty associated with studying them. Since exosomes are not the only extracellular vesicles (these include also for instance micro vesicles^[7]), the exosomes need to be separated from the rest. However, since there is a debate ongoing in the community with regards to what criteria an extracellular vesicle must fulfill in order to be accounted as an exosome, this separation is challenging. However, using the postulated (but existing, see Fig. 5.1) setup, one could sort an exosome-containing sample, linked to a supported membrane, into different size ranges and using for instance a fluorescently labeled antibody, visualize their content of a specific protein. The advantage here is that both these experiments can be done independently, which is not possible using any commercially available technique. In doing so, one could deduce whether exosome-specific markers are more or less prevalent in certain size ranges.

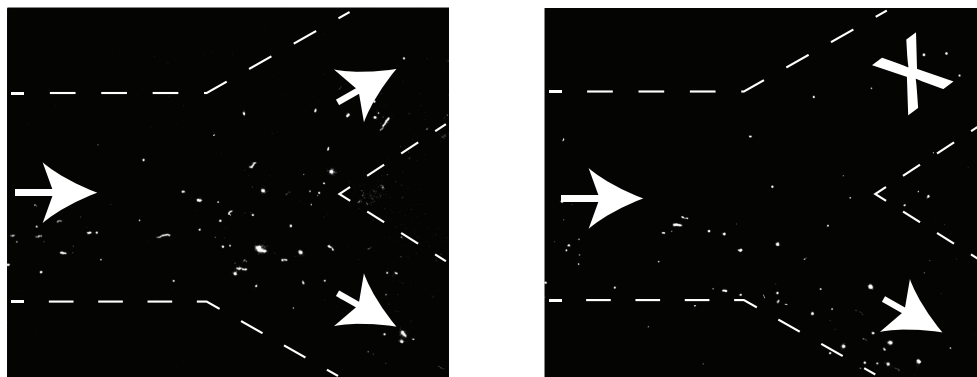


Fig. 5.1: Proof of concept “sorting” of vesicles. In the left figure, both outlets (on the right hand side of the figure) are open and vesicles are free to choose either outlet. In the right figure, the upper outlet is closed and the vesicles are thus forced to take the lower outlet. The switching is done by computer-controlled valves.

Exosomes, however, are not the only type of biological nanoparticles that could be size characterized in a similar way. While capsid viruses are known by transmission electron microscope studies (TEM) to be highly monodisperse,^[126] they also display a large sample heterogeneity with regards to lipids and proteins on the surface.^[127] Further, it is known that only a subset of the viruses are infectious.^[127] Once again, using the proposed technique and the unique possibility to perform both size characterization and functionality tests on the same batch in series that it provides, it can be determined if the sample heterogeneities in surface populations on the virus’ correlate with their size.

Size is of course not the only sorting criterion. Drawing parallels to fluorescence activated cell sorting (FACS) a type of flow cytometry,^[128] one can envision sorting based on color of the light scattered off of nanoparticles. For example, as discussed in chapter 3.1, metal nanoparticles have a LSPR, and the wavelength of this depends on the dielectric function of the metal and the environment of the nanoparticle, the size of the particle and its aspect ratio. Thus, many different colors of nanoparticles can be synthesized. Using a range of nanoparticles with different LSPR wavelengths, carrying different antibody modifications, multiple proteins can be targeted and sorted simultaneously, analogous to FACS, once again achieving enrichment/purification of membrane proteins without the need for detergent solubilization.

Another enticing future prospect is the membrane environment change, briefly explored in paper III, that the method facilitates, for studying for instance the effect of membrane composition on the activity of a membrane protein. One advantage over similar studies previously performed, *e.g.* by Kalvodova *et al.*^[129], is the internal reference provided by the system always providing a reference value. Also, moving a membrane protein from a crude cell-derived membrane to another membrane environment in this way, without detergent solubilization, means that the risk of ligand or cofactor loss is minimized.

Acknowledgements

First and foremost, I want to thank my PhD supervisor, *professor Fredrik Höök* and co-supervisors and mentors *Peter Jönsson*, *Anders Lundgren* and *Stephan Block* for your support and never-ending enthusiasm. How they manage, I can't comprehend, but I am thankful.

The people that I've been working with on both successful and failed projects.

All coworkers in the division of biological physics for fruitful discussions particularly during coffee breaks. *Thomas Olsson* and *Björn Agnarsson* deserve special mention for having had the dubious pleasure of sharing office with me and my keyboards.

Karin and *Greta*, my wonderful wife and daughter. My darlings. You are perfect. I love you.

My family and in-laws for your love and support.

Professor Eiiti Wada for designing the keyboard on which this thesis was typed.

My apologies if I have inadvertently omitted anyone to whom acknowledgement is due.

In the end, none of the above mentioned can be held responsible for what is written in this report, for that I take full responsibility. Having said that, the people mentioned above should take full credit for their contribution to my work, where there are errors, omissions and over-simplifications, it is probably because I did not heed their advice fully enough.

Thank you.

Bibliography

- [1] Alberts, B. *et al.* *Molecular Biology of the Cell* (Garland Science, New York, NY, 2007), 5. edn.
- [2] Lundstrom, K. *Cell. Mol. Life Sci.* **63**, 2597–2607 (2006).
- [3] Anfinsen, C. B. *Science* **181**, 223–230 (1973).
- [4] Poo, M. & Robinson, K. R. *Nature* **265**, 602–605 (1977).
- [5] Axelrod, D. Chapter 9: Total Internal Reflection Fluorescence Microscopy. In Taylor, D. L. & Wang, Y.-L. (eds.) *Fluorescence Microscopy of Living Cells in Culture Part B. Quantitative Fluorescence Microscopy–Imaging and Spectroscopy*, vol. 30 of *Method. Cell Biol.*, 245–270 (Academic Press, 1989).
- [6] Lequin, R. M. *Clin. Chem.* **51**, 2415–2418 (2005).
- [7] Raposo, G. & Stoorvogel, W. *J. Cell. Biol.* **200**, 373–383 (2013).
- [8] Israelachvili, J. N. *Intermolecular and Surface Forces* (Academic Press, Burlington, MA, 2011), 3. edn.
- [9] Jones, R. A. L. *Soft Condensed Matter* (Oxford University Press, Oxford, 2002), 1. edn.
- [10] Mueller, P., Rudin, D. O., Tien, H. T. & Wescott, W. C. *Nature* **194**, 979–980 (1962).
- [11] Tien, H. T., Carbone, S. & Dawidowicz, E. A. *Nature* **212**, 718–719 (1966).
- [12] Heron, A. J., Thompson, J. R., Mason, A. E. & Wallace, M. I. *J. Amer. Chem. Soc.* **129**, 16042–16047 (2007).
- [13] Keller, C. A. & Kasemo, B. *Biophys. J.* **75**, 1397–1402 (1998).
- [14] Groves, J. T., Ulman, N., Cremer, P. S. & Boxer, S. G. *Langmuir* **14**, 3347–3350 (1998).
- [15] Reviakine, I. & Brisson, A. *Langmuir* **16**, 1806–1815 (2000).
- [16] Reimhult, E., Höök, F. & Kasemo, B. *Langmuir* **19**, 1681–1691 (2003).
- [17] Hope, M. J., Bally, M. B., Webb, G. & Cullis, P. R. *Biochim. Biophys. Acta* **812**, 55–65 (1985).
- [18] MacDonald, R. C. *et al.* *Biochim. Biophys. Acta* **1061**, 297–303 (1991).

- [19] Huang, C. H. *Biochemistry* **8**, 344–352 (1969).
- [20] Johnson, S. M., Bangham, A. D., Hill, M. W. & Korn, E. D. *Biochim. Biophys. Acta* **233**, 820–826 (1971).
- [21] Brian, A. A. & McConnell, H. M. *Proc. Nat. Acad. Sci. USA* **81**, 6159–6163 (1984).
- [22] McConnell, H. M., Watts, T. H., Weis, R. M. & Brian, A. A. *Biochim. Biophys. Acta* **864**, 95–106 (1986).
- [23] Keller, C., Glasmästar, K., Zhdanov, V. P. & Kasemo, B. *Phys. Rev. Lett.* **84**, 5443–5446 (2000).
- [24] Zhdanov, V. P. & Kasemo, B. *Langmuir* **17**, 3518–3521 (2001).
- [25] Castellana, E. T. & Cremer, P. S. *Surf. Sci. Rep.* **61**, 429–444 (2006).
- [26] Seifert, U. *Adv. Phys.* **46**, 13–137 (1997).
- [27] Reimhult, E., Kasemo, B. & Höök, F. *Int. J. Mol. Sci.* **10**, 1683–1696 (2009).
- [28] Fuhrmans, M. & Müller, M. *Langmuir* **29**, 4335–4349 (2013).
- [29] Richards, M. J. *et al. Langmuir* (2016).
- [30] Bayerl, T. M. & Bloom, M. *Biophys. J.* **58**, 357–362 (1990).
- [31] Johnson, S. J. *et al. Biophys. J.* **59**, 289–294 (1991).
- [32] König, B. W. *et al. Langmuir* **12**, 1343–1350 (1996).
- [33] Kiessling, V. & Tamm, L. K. *Biophys. J.* **84**, 408–418 (2003).
- [34] Ajo-Franklin, C. M., Yoshina-Ishii, C. & Boxer, S. G. *Langmuir* **21**, 4976–4983 (2005).
- [35] Reimhult, E. & Kumar, K. *Trends Biotech.* **26**, 82–89 (2008).
- [36] Majewski, J. *et al. Biophys. J.* **75**, 2363–2367 (1998).
- [37] Tanaka, M. & Sackmann, E. *Nature* **437**, 656–663 (2005).
- [38] Sackmann, E. *Science* **271**, 43–48 (1996).
- [39] Schmitt, J., Danner, B. & Bayerl, T. M. *Langmuir* **17**, 244–246 (2001).
- [40] Przybylo, M. *et al. Langmuir* **22**, 9096–9099 (2006).
- [41] Seu, K. J. *et al. Biophys. J.* **92**, 2445–2450 (2007).
- [42] Tamm, L. K. *Biochemistry* **27**, 1450–1457 (1988).
- [43] Almeida, P. F. F., Vaz, W. L. C. & Thompson, T. E. *Biochemistry* **31**, 6739–6747 (1992).

- [44] Böckmann, R. A., Hac, A., Heimburg, T. & Grubmüller, H. *Biophys. J.* **85**, 1647–1655 (2003).
- [45] Filippov, A., Orädd, G. & Lindblom, G. *Chem. Phys. Lipids* **159**, 81–87 (2009).
- [46] Bayburt, T. H., Grinkova, Y. V. & Sligar, S. G. *Nano Lett.* **2**, 853–856 (2002).
- [47] Simonsson, L. *et al. J. Amer. Chem. Soc.* **133**, 14027–14032 (2011).
- [48] Plant, A. L. *Langmuir* **9**, 2764–2767 (1993).
- [49] Tamm, L. K. & McConnell, H. M. *Biophys. J.* **47**, 105–113 (1985).
- [50] Granéli, A., Rydström, J., Kasemo, B. & Höök, F. *Langmuir* **19**, 842–850 (2003).
- [51] Sundh, M., Svedhem, S. & Sutherland, D. S. *Phys. Chem. Chem. Phys.* **12**, 453–460 (2010).
- [52] Simonsson, L. & Höök, F. *Langmuir* **28**, 10528–10533 (2012).
- [53] Hardy, G. J. *et al. J. Mater. Chem.* **22**, 19506–19513 (2012).
- [54] Hardy, G. J., Nayak, R. & Zauscher, S. *Curr. Opin. Colloid Interface Sci.* **18**, 448–458 (2013).
- [55] Dodd, C. E. *et al. Biointerphases* **3**, FA59 (2008).
- [56] Costello, D. A. *et al. Langmuir* **29**, 6409–6419 (2013).
- [57] Pace, H. *et al. Anal. Chem.* **87**, 9194–9203 (2015).
- [58] Pace, H. "Private Communication" (2015).
- [59] Einstein, A. *Ann. Phys.* **322**, 549–560 (1905).
- [60] Sutherland, W. *Phil. Mag.* **9**, 781–785 (1905).
- [61] Smoluchowski, M. *Ann. Phys.* **326**, 756–780 (1906).
- [62] Smith, J. L. *Am. J. Sci. Arts* **14**, 233–241 (1852).
- [63] Thomson, N. L., Pearce, K. H. & Hsieh, H. V. *Eur. Biophys. J.* **22**, 367–378 (1993).
- [64] Lakowicz, J. R. *Principles of Fluorescence Spectroscopy* (Springer, New York, NY, 2006), 3. edn.
- [65] Ambrose, P. W., Goodwin, P. M. & Nolan, J. P. *Cytometry* **36**, 224–231 (1999).
- [66] Hecht, E. *Optics* (Addison-Wesley, San Francisco, CA, 2001), 4. edn.
- [67] Dulkeith, E. *et al. Phys. Rev. Lett.* **89**, 203002 (2002).
- [68] Schneider, G. & Decher, G. *Nano Lett.* **6**, 530–536 (2006).
- [69] Olsson, T., Zhdanov, V. P. & Höök, F. *J. Appl. Phys.* **118**, 064702 (2015).

- [70] Valeur, B. & Berberan-Santos, M. N. *Molecular fluorescence: principles and applications* (Wiley-VCH, Weinheim, Germany, 2012), 2. edn.
- [71] Liebman, P. A. & Entine, G. *Science* **185**, 457–459 (1974).
- [72] Poo, M. M. & Cone, R. A. *Nature* **247**, 438–441 (1974).
- [73] Axelrod, D. *et al. Biophys. J.* **16**, 1055–1069 (1976).
- [74] Reits, E. A. J. & Neefjes, J. J. *Nat. Cell Biol.* **3**, E145–E147 (2001).
- [75] Lippincott-Schwartz, J., Snapp, E. & Kenworthy, A. *Nat. Rev. Mol. Cell Biol.* **2**, 444–456 (2001).
- [76] Carrero, G. *et al. Methods* **29**, 14–28 (2003).
- [77] Gambin, Y. *et al. Proc. Nat. Acad. Sci. USA* **103**, 2098–2102 (2006).
- [78] Ausserré, D. & Valignat, M.-P. *Nano Lett.* **6**, 1384–1388 (2006).
- [79] Ausserré, D. & Valignat, M.-P. *Opt. Express* **15**, 8329–8339 (2007).
- [80] Nafday, O. A., Lowry, T. W. & Lenhert, S. *Small* **8**, 1021–1028 (2012).
- [81] Gunnarsson, A. *et al. Anal. Chem.* **84**, 6538–6545 (2012).
- [82] Mie, G. *Ann. Phys.* **330**, 377–445 (1908).
- [83] Maier, S. A. *Plasmonics: Fundamentals and Applications* (Springer, New York, NY, 2007).
- [84] Agnarsson, B. *et al. ACS Nano* **9**, 11849–11862 (2015).
- [85] Xia, Y. & Whitesides, G. M. *Annu. Rev. Mater. Sci.* **28**, 153–184 (1998).
- [86] McDonald, J. C. *et al. Electrophoresis* **21**, 27–40 (2000).
- [87] Jönsson, P. *et al. Proc. Nat. Acad. Sci. USA* **109**, 10328–10333 (2012).
- [88] Jönsson, P. & Höök, F. *Langmuir* **27**, 1430–1439 (2011).
- [89] Day, M. A. *Erkenntnis* **33**, 285–296 (1990).
- [90] Jönsson, P., Beech, J. P., Tegenfeldt, J. O. & Höök, F. *J. Amer. Chem. Soc.* **131**, 5294–5297 (2009).
- [91] Jönsson, P., Gunnarsson, A. & Höök, F. *Anal. Chem.* **83**, 604–611 (2011).
- [92] Jönsson, P. & Jönsson, B. *Langmuir* **31**, 12708–12718 (2015).
- [93] Stelzle, M., Miehlich, R. & Sackmann, E. *Biophys. J.* **63**, 1346–1354 (1992).
- [94] Kam, L. & Boxer, S. G. *Langmuir* **19**, 1624–1631 (2003).
- [95] Daniel, S. *et al. J. Am. Chem. Soc.* **129**, 8072–8073 (2007).

- [96] Groves, J. T., Wülfing, C. & Boxer, S. G. *Biophys. J.* **71**, 2716–2723 (1996).
- [97] Cheetham, M. R. *et al. Soft Matter* **8**, 5459–5465 (2012).
- [98] Liu, C. *et al. Anal. Chem.* **83**, 7876–7880 (2011).
- [99] Hennig, M. *et al. Lab Chip* **9**, 3050–3053 (2009).
- [100] Neumann, J., Hennig, M., Wixforth, A. & Manus, S. *Nano Lett.* **10**, 2903–2908 (2010).
- [101] Chao, L., Richards, M. J., Hsia, C. Y. & Daniel, S. *Anal. Chem.* **85**, 6696–6702 (2013).
- [102] Hu, S. K. *et al. Sc. Tech. Adv. Mater.* **14**, 044408 (2013).
- [103] Johansson, B., Olsson, T., Jönsson, P. & Höök, F. *Soft Matter* **9**, 9414–9419 (2013).
- [104] Jönsson, P., Jonsson, M. P., Tegenfeldt, J. O. & Höök, F. *Biophys. J.* **95**, 5334–5348 (2008).
- [105] Park, S., Yang, P., Corredor, P. & Weaver, M. J. *J. Am. Chem. Soc.* **124**, 2428–2429 (2002).
- [106] Park, Y. K. & Park, S. *Chem. Mater.* **20**, 2388–2393 (2008).
- [107] van der Pol, E. *et al. Nano Lett.* **14**, 6195–6201 (2014).
- [108] Jönsson, P. *Properties and applications of shear-driven lipid bilayers*. Ph.D. thesis, Chalmers University of Technology (2010).
- [109] Zhang, R.-G. *et al. J. Mol. Biol.* **251**, 563–573 (1995).
- [110] De Haan, L. & Hirst, T. R. *Mol. Membr. Biol.* **21**, 77–92 (2005).
- [111] Terrettaz, S., Stora, T., Duschl, C. & Vogel, H. *Langmuir* **9**, 1361–1369 (1993).
- [112] Johansson, B., Höök, F., Klenerman, D. & Jönsson, P. *Chem. Phys. Chem.* **15**, 486–491 (2014).
- [113] Kato, K. *et al. J. Exp. Med.* **176**, 1241–1249 (1992).
- [114] Wilkins, A., Yang, W. & Yang, J. *Curr. Protein Pept. Sc.* **4**, 367–373 (2003).
- [115] Saxton, M. J. & Jacobson, K. *Annu. Rev. Bioph. Biom.* **26**, 373–399 (1997).
- [116] Yoshina-Ishii, C. *et al. Langmuir* **22**, 5682–5689 (2006).
- [117] Johansson Fast, B. *et al. Detergent free affinity purification of membrane proteins in supported native membranes*. In manuscript (2016).
- [118] Cole, S. L. & Vassar, R. *Curr. Alzheimer Res.* **5**, 100–120 (2008).
- [119] Saffman, P. G. & Delbrück, M. *Proc. Natl. Acad. Sci.* **78**, 3111–3113 (1975).

Bibliography

- [120] Block, S., Zhdanov, V. P. & Höök, F. Quantification of multivalent interactions by tracking single biological nanoparticle mobility on a lipid membrane. Submitted (2016).
- [121] Block, S. *et al.* Two-dimensional flow nanometry of biological nanoparticles for accurate determination of size and emission intensity. In manuscript (2016).
- [122] Lundgren, A. *et al.* *Part. Part. Syst. Char.* **31**, 209–218 (2014).
- [123] Mathivanan, S., Fahner, C. J., Reid, G. E. & Simpson, R. J. *Nucleic Acids Res.* **40**, D1241–D1244 (2012).
- [124] Valadi, H. *et al.* *Nat. Cell Biol.* **9**, 654–659 (2007).
- [125] Balaj, L. *et al.* *Nat. Comm.* **2**, 180 (2010).
- [126] Hu, Y. *et al.* *Biophys. J.* **94**, 1428–1436 (2008).
- [127] Gaudin, R. & Barteneva, N. S. *Nat. Comm.* **6**, 6022 (2015).
- [128] Julius, M. H., Masuda, T. & Herzenberg, L. A. *Proc. Natl. Acad. Sci.* **69**, 1934–1938 (1972).
- [129] Kalvodova, L. *et al.* *J. Biol. Chem.* **280**, 36815–36823 (2005).